
AFRICA CENTER OF EXCELLENCE FOR WATER MANAGEMENT

ADDIS ABABA UNIVERSITY


# Synthesis and characterization of Graphitic Carbon Nitride for the removal of Methylene blue dye from wastewater

By

EYERUSALEM AYALKIBET

A thesis submitted to the African Centre of Excellence for Water Management (ACEWM) in partial fulfilment of the requirement for a Master's Degree in Water Management (Water and Wastewater Technology) of Addis Ababa University

October 2021

Addis Ababa, Ethiopia

Synthesis and characterization of Graphitic Carbon Nitride for the removal of dye from wastewater

By
EYERUSALEM AYALKIBET

A thesis submitted to the African Centre of Excellence for Water Management (ACEWM) in partial fulfilment of the requirement for a Master's Degree in Water Management (Water and Wastewater Technology) of Addis Ababa University.

Advisor

Name: Dr. Shimelis Kebede Signature_____ Date_____

Co-Advisor

Name: Dr. Hailemariam Gebru Teka Signature_____ Date_____

October 2021

ADDIS ABABA UNIVERSITY

AFRICA CENTER OF EXCELLENCE FOR WATER MANAGEMENT

Thesis Approval Form

APPROVED BY BOARD OF EXAMINERS

This is to certify that we the undersigned, have examined this MSc thesis entitled "Synthesis and characterization of Graphitic Carbon Nitride for the removal of dye from waste water" and that in our opinion; it is fully adequate, in scope and quality, as an MSc thesis for the degree of Master of Science in Water Management (Water and Wastewater Technology).

Advisor

Name: Dr. Shimelis Kebede Signature_____ Date_____

Co-Advisor

Name: Dr. Hailemariam Gebru Teka Signature_____ Date_____

External Examiner: Dr. Nigus Gabbiye Habtu

Signature……. ……..…….. Date:……..

Internal Examiner: Dr. Beteley Tekola

Signature……. ……..…….. Date:……..

Chairperson: ……..

Signature……. ……..…….. Date:……..

Statement of the author

I, EYERUSALEM AYALKIBET, declare that this research report is my original effort and work and to the best of my knowledge, the findings have never been previously presented to the Addis Ababa University or elsewhere for the award of any academic qualification. Where assistance was sought, it has been accordingly acknowledged. The findings, interpretations and conclusions expressed in this study neither reflect the views of the Addis Ababa, African Centre of Excellence for Water Management (ACEWM), nor those of the individual members of the MSc Examination Committee.

Signature…….…… Date:……..

Acknowledgement

First of all, I would like to thank the almighty GOD for all the strength and courage to overcome challenges. I also would like to express my deepest appreciation to my advisor Dr. Shimelis Kebede for his valuable advice on this research. In directing and correcting the methods I used in the process and his full support in analyzing the outcome of the investigation at the starting and direction of logical esteem all through the completion of my theses. In addition, many thanks to my Co-Advisor Dr. Hailemariam Gebru Teka for his helpful advice to apply different approaches, frequent follow up, and come up with the best result of the intended project. I would like to appreciate to the School of Chemical and Bioengineering staff members, particularly Mr. Hintsa Selesse for his assistance on experimental works. Finally, I would like to extend my deepest gratitude to my parents and my two children (Amen and Yohanna) for their assistance and understanding that I worked on the research. I commit this work to my two children.

Abstract

Graphitic carbon nitride (g-$C_3N_4$) has received much attention for its potential application in pollutant degradation due to its unique optical and physicochemical properties. Various technologies have been developed to remove pollutants, but efficient and economical wastewater treatment remains a challenge in terms of energy and treatment costs. Herein, a visible-light active and robust semiconductor, g-$C_3N_4$ was synthesized from low-cost precursors like urea using pyrolysis at 500 ºC and 550 ºC. Herein, the as-synthesized material was characterized by UV-vis spectrophotometer to show the catalyst optical characteristics and can consider the best reaction temperature to obtain graphitic carbon nitride with maximum visible light response. Likewise, Fourier transform infrared spectroscopic (FT-IR) analysis was required to confirm the structure and the presence of C=N or functional groups. Sample morphology and structure were characterized by scanning electron microscopy (SEM), nitrogen adsorption-desorption isotherm analysis, X-ray diffraction (XRD). In this research important photocatalytic degradation procedure, the factors that affect the efficiency of photocatalytic degradation of organic pollutants, and the effects of different reaction parameters are highlighted. The photo-catalytic degradation of methylene blue (MB) was evaluated under visible light irradiation. As prepared sample having a specific surface area of 54.9 $m^2$/g, the photo-catalytic activity under visible light irradiation performed and it takes 120 min for 96% degradation methylene blue. The Freundlich and Langmuir adsorption models were used to elucidate the adsorption efficiency of g-$C_3N_4$. The kinetic data depicts the pseudo first, second, and inter-particle diffusion model. Adsorption and kinetic isotherm showed that the adsorption process could be well described by pseudo-first - order kinetic model, with an adsorption capacity of 552 mg MB per gram adsorbent determined by Langmuir isotherm. These results provide some idea for the design and development of g-$C_3N_4$-based high activity photo catalysts, which is an effective strategy for organic pollutants degradation and solar energy conversion.

Keywords: Graphitic carbon nitride, photocatalyst, pollutant degradation, adsorption isotherm, kinetics

# Table of Contents

# Appendixes

# List of tables

# List of figures

# List of Acronyms

| | |
|---|---|
| ACEWM | AFRICA CENTER OF EXCELLENCE FOR WATER MANAGEMENT |
| G-$C_3N_4$ | GRAPHITIC CARBON NITRIDE |
| MB | METHYLENE BLUE |
| XRD | X-RAY DIFFRACTION |
| FTIR | FOURIER TRANSFORM INFRARED SPECTROSCOPY |
| SEM | SCANNING ELECTRON MICROSCOPY |
| PL | PHOTOLUMINESCENCE |
| UV-vis | UV-VISIBLE SPECTROPHOTOMETER |
| BET | BRUNAUER-EMMETT-TELLER |
| WHO | WORLD HEALTH ORGANIZATION |
| RSM | RESPONSE SURFACE METHODOLOGY |
| DOE | DESIGHN OF EXPERIMENT |
| RhB | RHODAMINE B |
| TOC | TOTAL ORGANIC CARBON |

## 1. Introduction

Graphitic carbon nitride (g-$C_3N_4$) has received much attention in recent years due to its unique optical and physicochemical properties. In all other applications such as energy conversion, sensing, bioimaging, g-$C_3N_4$ is mainly used as a photocatalyst for water splitting, $CO_2$ reduction, and pollutant degradation due to its tiny bandgap and ability to capture light. With the rapid growth of the world's population, the development of industrialization is related to the increase in the amount of wastewater produced. Currently, the release of non-biodegradable toxic organic and inorganic compounds pollutes water bodies and causes shortages of drinking water. According to the statistical analysis report of UNESCO (2017) stated that about 80% of wastewater is discharged into the ecosystem without any treatment, which pollutes most water bodies[1]. In this sense, the excessive release of anthropogenic pollutants produced by industrial uses such as phenolic compounds, heavy metals, and synthetic dyes leads to the deterioration of water quality and harmful effects on living organisms.

Various technologies have been developed to remove pollutants, but efficient and economical wastewater treatment remains a challenge in terms of energy and treatment costs. Some conventional technologies, such as flocculation, coagulation, reverse osmosis, ion exchange, adsorption, precipitation, membrane filtration, chlorination, neutralization, photoelectron chemistry, precipitation, etc., have been used for the treatment of wastewater discharged from different sources[2]. These techniques have some disadvantages, for example, flocculation and coagulation are used to remove insoluble compounds from water, requiring additional chemicals that can be toxic. Similarly, membrane filtration reverse osmosis removes excess anions and cations but tends to remove solvents (phenols and halogenated compounds, benzene, pesticides) and other types of pollutants such as organic pollutants there is not[3]. It is worth noting that the above methods are limited by the requirements of high operating costs, low energy efficiency, and sophisticated types of equipment.

Therefore, it is necessary to develop new technology that can efficiently remove pollutants from wastewater at a low cost and in an environmentally friendly manner. Organic pollutants such as dyes, pesticides, and pharmaceutical wastes are widespread in wastewater and are very harmful to biological safety and ecosystems. Persistent and toxic organic pollutants, especially pesticides,

have long half-lives. Green Catalyst Technology as Photocatalysts can decompose almost all organic pollutants without choice.

### 1.1 Statement of problem

Dye wastewater is a common type of water pollutant and a concern for wastewater treatment. The effluent is from different types of industries, like food, printing, textiles, and cosmetics, and possesses a profound threat to the environment due to its toxicity and lack of biodegradability. Though decolorization and detoxification of dye-containing wastewater need to be conducted before discharging wastewater into natural water bodies, most of the existing physical and chemical methods usually show high dye-removal efficiencies, high operational costs are required[4]. G-$C_3N_4$ is simple photo-catalytic technology makes dye waste water to be recyclable and intended for different water reuse applications minimize the pollution load on water bodies. A visible-light active and robust semiconductor, g-$C_3N_4$ was synthesized from low-cost precursors like urea.

Synthesis pathway and good selection of the template or dopant are essential for the complete and successful preparation of g-$C_3N_4$. According to the characteristics of the pollutants, the efficiency of photocatalysts/adsorbents is different. The purely prepared g-$C_3N_4$ material has a low surface area, which reduces its catalytic activity it is necessary to increase the surface area of the material. Wang et al. suggested under the same pyrolysis conditions, the surface area of (g-$C_3N_4$) sample (75$m^2$/gm) from urea is higher than that of samples prepared directly from thiourea (27 $m^2$/gm) and other precursors. Because of formation of porous structure due to release of gases ($NH_3$, $H_2O$) during thermal condensation reaction of urea precursor. Dong et al. prepared the g-$C_3N_4$ using urea via a facile template-free, studies the effects of pyrolysis time on the microstructure and activity of g-$C_3N_4$ photocatalyst. They suggested that the surface areas of the photocatalyst can be significantly increased by just prolonging the pyrolysis time to 240 minutes at under 550°C. high surface area (288$m^2$/gm). Yuliati et al. also applied templating strategy to increase the surface area of g-$C_3N_4$ (224$m^2$/gm) using urea as precursor. The resultant (g-$C_3N_4$) showed markedly enhanced visible light photocatalytic activities toward hydrogen evolution or pollutants degradation. In other research, Song X, Yang Q, Yin M, Tang D, Zhou L. a novel g-$C_3N_4$ surface area of 114$m^2$/gm allowed the repetitive adsorption of the rhodamine B (RhB) dye

with strong adsorption capability and efficient photocatalytic activity was prepared by heating urea via a facile method, the addition of $N_2$ at 300 ◦C was stopped, complete photocatalytic degradation upon light irradiation in 20 min.

This study was including synergistic adsorption-photocatalysis processes of graphitic carbon nitride for removal of MB dye by applying RSM method based on Box-Behnken design. As key factor variables Adsorbent dose, pH, Adsorbate concentration and temperature were used to analyze the influence of such different parameters. G-$C_3N_4$ helps to decolorize methylene blue (MB) a model pollutant, synthesized with urea as a precursor, under visible light irradiation[5]. For practical applications as catalysts/adsorbent understanding of the active-site structures of bulk g-CN as benchmark material and for comparison purpose crucially important, it is necessary to introduce well-controlled porous structures in the bulk g-$C_3N_4$ to obtain porous g-$C_3N_4$ and improve the efficiency of material[6]. The fundamentals of synergistic adsorptive and photocatalytic removal of contaminants briefly described using RSM approach for development and optimization of nano-photocatalysts. The results present by such approach has not been investigated in depth so far.

## 1.2 Research questions

1. What are the optimum parameters in the preparation of graphitic carbon nitride (g-$C_3N_4$) in order to improve surface area and crystallinity of the material?
2. What is the minimum requirement for graphitic carbon nitride as adsorbent and catalyst to be used in adsorption -degradation process?
3. What are the parameters and conditions to observe during integrated adsorption degradation of MB?

## 1.3 Objectives

### 1.3.1 General objective

The general objective of this study is to synthesis and characterize of graphic carbon nitride to use as adsorbent and visible light active photo-catalyst for the degradation of methylene blue.

### 1.3.2 Specific objectives

- ✓ To synthesize graphitic carbon nitride nano material using urea as precursor by simple pyrolysis then characterize the morphology and structure of the sample by SEM, BET, XRD and UV–vis spectrophotometer techniques.
- ✓ To determine the effect of different factors on adsorption and photocatalysis performance of methylene blue (MB).
- ✓ To investigate the interactive effect and removal kinetic model of integrated adsorption and degradation of MB.

## 1.4. Scope

First using law cost raw material to synthesize graphitic carbon nitride then describe the type of the material and characterizing the structural properties of graphitic carbon nitride using a series of measurement techniques depending on the techniques available. Then select best material, which has high integrated effect of adsorption and photo-catalytic activity for removal of dye waste water.

## 2. Literature review

### 2.1 Photo-catalysts

Photocatalytic materials have potential applications in the conversion of solar energy, the degradation of organic pollutants, the splitting of photocatalytic water to produce hydrogen, the reduction of carbon dioxide, and the synthesis of organic compounds. In the field of wastewater treatment, due to several advantages, photocatalytic degradation of pollutants is more advantageous than conventional methods. The process does not require non-renewable energy consumption because it is combined with sustainable solar energy. Photocatalytic technology is suitable for gas and water treatment and can degrade a variety of pollutants and toxic compounds without producing secondary pollutants. Furthermore, the photocatalyst can be easily synthesized from readily available precursors. The whole process is not only simple to conduct, low cost, and requires a relatively short process time, the method is sustainable for wastewater in a large-scale application[7].

Photocatalytic materials can be divided into four types depending on their band structure and composition including metal/nonmetal doped semiconductors with large band gap (such as C/N-doped $TiO_2$, N doped $(BiO)_2CO_3$), metal-containing semiconductors with narrow bandgap (such as $Bi_2WO_6$, $Bi_3NbO_7$, BiOBr), plasmonic noble metals (such as Au, Pt), and more. At present, a great deal of laboratory-scale research has been conducted on g-$C_3N_4$ photocatalysis, focusing on the development of metal-free photocatalysts such as $TiO_2$ g-$C_3N_4$, doped with ZnO, and carbonaceous materials. For instance, Liu et al. reported the large-scale preparation of g-$C_3N_4$ through pyrolysis of urea by applying ambient pressure, high temperature, and different time intervals as a photo-catalyst for visible light-assisted MB degradation[8]. G. Xin and Y. Meng employed cyanamide, dicyandiamide, and melamine as a precursor to synthesized g-$C_3N_4$ powder at 520°C using the pyrolysis method for photo-degrading experiments of methylene blue (MB)[9]. Several reports have concluded that to improve photo-catalytic or pollutant degeneration efficiency of bulk g-$C_3N_4$ material mixing with semiconductors and doping with metal or nonmetal is important. It is advisable to consider the selection mechanism of dopant compatibility and material properties.

## 2.2 Graphitic carbon nitride (g-$C_3N_4$)

g-$C_3N_4$ is one of the oldest polymer derivatives and manufactured by Berzelius and was named "melon" by Liebig in 1834, but it was not used as a heterogeneous metal-free catalyst until 2006, and was released as a new generation in 2009 g-$C_3N_4$ metal-free polymer photocatalyst[10]. Since then, the number of studies on the electrocatalytic and photocatalytic properties of graphite carbon nitride has continued to increase[11]. Among photocatalysts, graphite carbon nitride (g-$C_3N_4$) is of great importance as a photocatalyst for environmental pollution remediation due to its excellent physicochemical properties. g-$C_3N_4$ is a new kind of metal-free photocatalyst with good light absorption performance and small band-gap energy of 2.7 eV, which belongs to the region of visible light. The valence band (VB) and the conduction band (CB) of the g-$C_3N_4$ photocatalyst are 1.56 eV and 1.09 eV, respectively[2]. Development of visible-light-driven photocatalysts for environmental remediation solves future energy and environmental problems also for energy conversions, such as photodegradation of organic pollutants, photoelectric conversion, $H_2$ production, $CO_2$ activation, and other important catalytic reactions[12]. Most of the literature reports have been reported on approaching the synthesis of different modifications and elucidation of the structural composition of carbon nitride materials also Potential applications in energy conversion,[13] hydrogen[14], [15]and sensing[16], purification of contaminated water[17], in solar cell[18], as sustainable enzymatic synthesis[19].

In recent years, g-$C_3N_4$ has attracted a lot of attention due to the more stable allotrope of carbon nitride. This allows it to be used directly as a multifunctional metal-free heterogeneous catalyst in sustainable chemistry, for example in hydrocarbon[20], oxidation, and water splitting[21]. Doping the carbon nitride matrix or surface with atoms or functional groups such as boron, fluorine, sulfur, etc., undoubtedly greatly improves its photocatalytic performance.

## 2.3 Methods of Graphitic carbon nitride (g-$C_3N_4$) production

Various synthesis techniques have been investigated such as chemical vapor deposition, solvothermal, Sono-chemical, and thermal condensation. Specifically, nitrogen-rich compounds such as urea, cyanamide, dicyanamide, melamine and thiourea are commonly used as a starting material in the thermal condensation technique. This technique is the most attractive due to its

cheap cost, operationally simple, and earth-abundant precursors[1]. For example, urea as precursor

very cheap thereby the synthesis of g-$C_3N_4$ using the thermal condensation method is extremely simple. Unlike urea, some other starting materials are toxic to humans and the environment, and some are unstable or difficult to synthesize on a large scale. Wang et al. reported that under the same pyrolysis conditions, the surface area of g-$C_3N_4$ sample (75 $m^2/g$) from urea is higher than that of samples prepared directly from thiourea (27 $m^2/g$) and other precursors. Because of formation of porous structure due to release of gases ($NH_3$ and $H_2O$) during thermal condensation reaction of urea precursor[7]. Accordingly; g-$C_3N_4$ was synthesized by thermal treatment of urea (20g) in a crucible, with aluminum cover under ambient pressure. The urea was placed in a Muffle Furnace and calcine at 500 and 550$^o$c pyrolysis time of 3 and 4 hours to complete the reaction then got four pale-yellow powder samples.

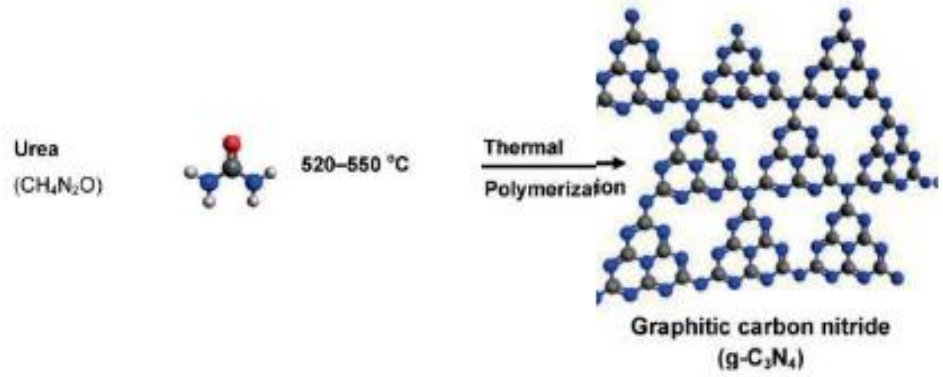


Figure 2. 1 Schematic representation of a synthesis of g-$C_3N_4$ [1]

Table 2. 1 G-$C_3N_4$ material coupling with other dopants

| Methods | Principle | Advantages | Disadvantages |
|---|---|---|---|
| Metal doping | Doping of various metallic species such as alkali metals, rare earth metals, and noble metals into g-$C_3N_4$ | Bandgap narrowing, surface area improvement, charge separation, and fine-tuning the band structure | Can often cause secondary pollution due to the leaching of the metal ions |
| Non-metal doping | Doping g-$C_3N_4$ with nonmetals | No secondary pollution, improve visible light absorption and charge separation | Non-metal species does not take part in charge transportation hence recombination centers are formed |
| Noble metal deposition | Deposition of noble metal nanoparticles such as Cu, Pt, Au, and Pd on g-$C_3N_4$ | Metal content positively influence the photocatalytic activity until the optimum loading is reached | Beyond the optimum metal loading, the excess metal ions act as recombination centers for the electron/hole pairs |
| Hybridizing g-$C_3N_4$ with carbon nanomaterials (CNM) | Carbon nanomaterial such as carbon nanotubes (CNTs), carbon nanospheres (CNS), graphene oxide (GO), and reduced graphene oxide RGO) | High thermal, electronic conductivity, remarkable adsorption properties for organic and inorganic compounds | Excess CNM (i.e . RGO) facilitate adsorption of large amounts of the dye molecules onto the catalyst surface thereby reducing light penetration to the photocatalyst |
| Coupling g-$C_3N_4$ with semiconductor | Coupling two or more semiconductors to form a semiconductor heterojunction improved stability, visible light utilization, charge separation and transfer, and more efficient formation of the oxidizing species | Improved stability, visible light utilization, charge separation, and transfer, and more efficient formation of the oxidizing species | Difficult to find a proper semiconductor photocatalyst with a suitable band edge position |

## 2.4 Mechanisms in photo-catalytic reactions

The photocatalyst is characterized as a combination of catalysis and photochemistry, where the absorption of photon energy from light by the catalyst changes the rate of reaction that exists during the photoreaction process. Therefore, a photocatalyst is a material that changes the rate of a chemical reaction when exposed to light. This phenomenon is called photocatalysis[1]. Initially, the g-$C_3N_4$ photocatalyst will absorb the energy of photons with energy equal to or prominent than its bandgap energy when exposed to the light of the required wavelength or sufficient energy, which makes the energy of photons be absorbed by electrons ($e^-$) in the valence band (VB) and become excited and migrate to the conduction band (CB). In this process, a hole ($h^+$) is created in the valence band. This process leads to the formation of a photoexcited state and produces $e^-$ and $h^+$ pairs. The excited electron is used to reduce the acceptor, and the hole is used for the oxidation of the donor molecule.

$$g\text{-}C_3N_4 + hV \longrightarrow e^- CB\ (g\text{-}C_3N_4) + h^+ VB\ (g\text{-}C_3N_4)$$

Then, the electron will be excited and leave photo-generated holes ($h^+$) in the valence band. The photo-generated holes and photoexcited electrons will migrate to the surface of the photo-catalyst and be trapped there. The photo-generated holes then react with adsorbed water to produce strong oxidizing $^{\cdot}OH$ radicals whereas the photo-excited electrons react with adsorbed oxygen to generate $^{\cdot}O_2^-$ radicals. Further, react with the pollutant and subsequently degraded the pollutant[22]. Ultrathin g-$C_3N_4$ nanosheets derived from bulk g-$C_3N_4$ by exfoliation in methanol exhibit enhanced photocatalytic performance for methylene blue (MB) degradation. Tahir and co-workers also employed tubular g-$C_3N_4$ for MB and methyl orange (MO) photocatalytic degradation under visible light[23].

## 2.5 Key steps during pollutant degradation

Semiconductor photocatalysis is a very complex process that involves many reaction pathways that can responsible for the final decomposition of contaminants. This process can be summarized in five key steps that lead to the degradation of organic pollutants (Figure 2.2). The first step is the mass transfer of organic contaminants through the diffusion of the bulk solution

to the surface of the semiconductor. The second step is to adsorb the organic contaminants to the surface of the semiconductor and excite the semiconductor. The organic compounds are then degraded by oxidizing species. Subsequently, the desorption of the degraded products from the active surface of the photocatalyst takes place in step 4. Finally, the degradation products diffuse from the photocatalyst interface into the solution.

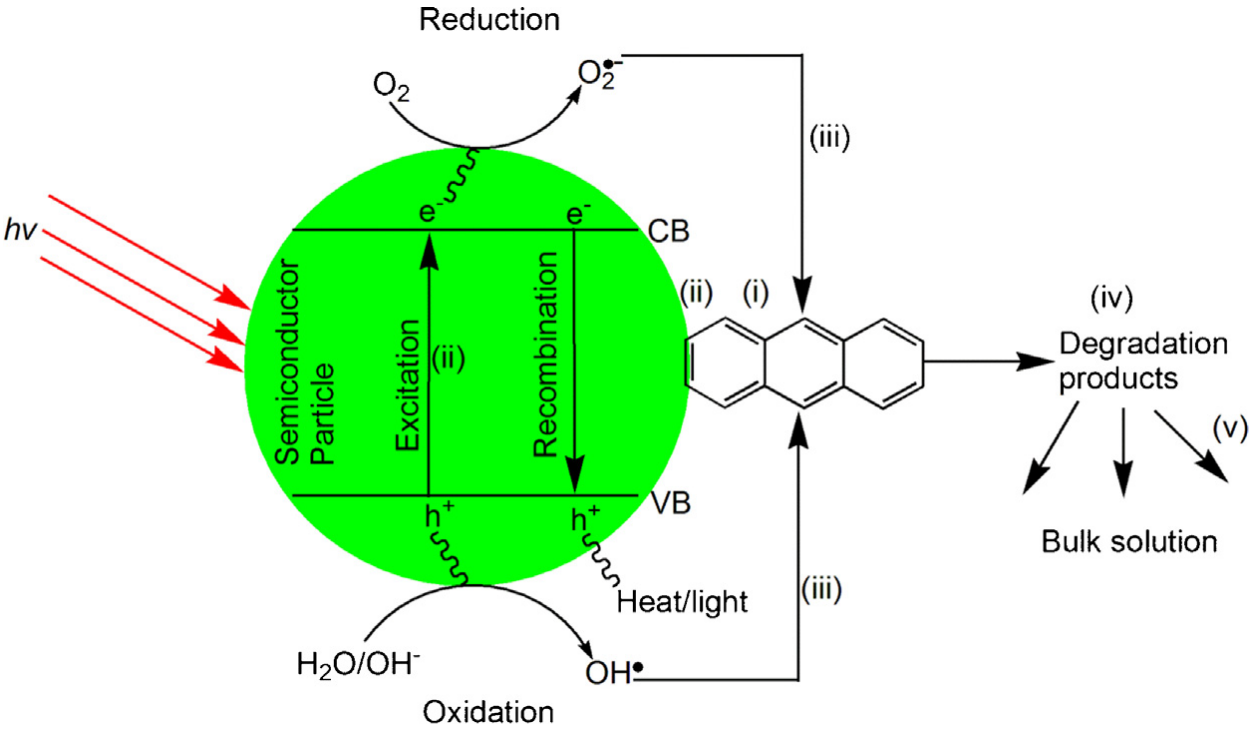


Figure 2. 2 Key steps in semiconductor photo-catalysis [24]

### 2.6 Enhancing photocatalytic activity

Yang et al. discussed some of the recent advancements towards hard and soft templating approaches for enhancing the photocatalytic activity of g-$C_3N_4$. Introducing heteroatoms (metal and non-metal doping) within the g-$C_3N_4$ framework, metal deposition, hybridizing with carbon nanomaterials, and coupling with other semiconductors have been the most attractive approaches towards fabricating heterostructures with improved photocatalytic activity[25]. Zhang et al. observed higher photocatalytic activity towards phenol and methylene blue (MB) over potassium doped g-$C_3N_4$ (K-g-$C_3N_4$) compared to bulk g-$C_3N_4$ under visible light irradiation. Potassium iodide was used as a K source and at 22%KI loading (22%K-g-$C_3N_4$) the highest activity was observed and it was 3.3 and 5.8 times higher than that of bulk g-$C_3N_4$ for phenol and MB

degradation, respectively[24]. Some selected materials coupling with graphitic carbon nitride given in table 2.1.

### 2.7 Kinetic studies

Photo-catalytic reaction kinetic can be well explained in the following steps. The first step is the absorption of light (i.e., photons) via photocatalysts (graphitic carbon nitride), and then the electrons get excited from a valence band to a conduction band or generation of electrons and hole pairs. The second step is the result of electron−hole pair recombination that occurs either in the core of the materials or on the surface of it, that is, related to the release of energy in the form of light emission. The third step can be attributed to the recombination of charges (electrons and holes) as the important process that controls the overall photo-catalyst efficiency after the absorption of photons (light energy). Charges (electrons or holes) that migrate onto the surface layer of the photo-catalysts do not go through the recombination and may indulge in other oxidation and reduction reactions with adsorbents such as oxygen, water, and any other inorganic or organic species [22].

For instance, take methylene blue as a model sample initial concentration of dye was mixed with g-$C_3N_4$ photocatalysts the material acts as a sensitizer for the light irradiated to stimulate the whole mechanism due to its electronic structure that is formed by a completely/partially filled valence band (VB) and conduction band (CB). When light is irradiated (photons) on the surface of graphitic carbon nitride catalyst, if this energy is equivalent to or more than band gap energy, then valence band electrons are excited to the conduction band, causing hole formation in the valence band. These holes could oxidize donor molecules and react with water molecules to form hydroxyl ions. The electrons present in the conduction band could actively react with dissolved oxygen ions to form superoxide ions, leading to redox reactions. Now, the electrons and holes present in CB and VB can go under the oxidation and reduction process with any species absorbed on the surface of the catalyst. Photo-catalytic studies could be done under visible light bulb irradiation at the sample surface under stirring conditions. Visible light irradiating time t reaches 40 min, the methylene blue dye in the as-prepared sample decays rapidly until a minimum percentage. The degradation rate and efficiency were determined in a pseudo-first-order reaction in a nonlinear regression of $\ln(C/Co) = -kt$[26].

The irradiation time and short adsorption equilibrium between MB and photo-catalyst are the most important design parameters that affect the performance of photo-degradation processes. The photocatalytic efficiency of the material determines by more efficient charge separation, rapid charge transfer, and reduced charge recombination.

### 2.8 Experimental conditions

The morphology and properties of $C_3N_4$ material strongly depend on the synthetic pathway, as well as on the precursor and different reaction parameters or experimental conditions including pH, the concentration of pollutant, dose of the adsorbent or photo-catalyst, and temperature to see the effect of such different reaction parameters on $C_3N_4$ materials refer previously reported researches. Dong et al. prepared the g-$C_3N_4$ using urea via a facile template-free and the surface areas of the photo-catalyst for removal of gaseous NO and aqueous RhB can be significantly increased to 288g/$m^2$ by just prolonging the pyrolysis time to 240 minutes at under 550°C. They suggested that increasing pyrolysis time enhances the surface area, increases pore volume enlarges the bandgap and decreases layer thickness that shortens the charge transport distance. They claimed the prepared surface area of g-$C_3N_4$ with this method is higher than g-$C_3N_4$ photo-catalyst prepared via templating method. The as-synthesized g-$C_3N_4$ material employed for photocatalytic removal of gaseous NO and aqueous RhB and showed efficient activity under visible light irradiation[7].

Particularly, a retainable pyrolysis-generated self-supporting atmosphere and the reaction temperature are the two vital parameters for the successful synthesis of g-$C_3N_4$. However, sometimes it is not possible to create a self-sufficient atmosphere because of several reasons which are not completely understood yet[18]. For materials synthesis, the use of temperature is the classic method to improve the reactivity of precursors and diffusion processes. In the case of carbon nitrides, the strong stability of the $N_2$ molecule competes with the formation of the Chemical bonds C-N that damages the elaboration of the required material[27].

## 3. Materials and methods

### 3.1 Materials

Crucible, muffle furnace, and Aluminum foil were used to synthesize g-$C_3N_4$. Urea, methylene blue chemical and reagents were used as received.

### 3.2 Apparatus

Beaker, volumetric flasks, micro pipettes, plastic and glass bottles, and magnetic stirrer are the apparatus used during experiments. Fourier transform infrared (FTIR) spectra were recorded using (Perkin Elmer, Spectrum 65FT-IR spectrophotometer) to analyze the functional groups present in the adsorbent, XRD characterization for crystallinity, surface morphology reveals by SEM, surface area determination by using BET method and photoelectronic property analyzed by PL. Solution pH was adjusted using pH meter. Magnetic stirrer for mixing of sample in the solution and self- made visible light(lamp) for photocatalytic reaction UV-spectrophotometer (x-ma 1200 UV/visible Spectrometer) for concentration and absorbance analyzer were used to evaluate the final MB concentration.

### 3.3 Methods

#### 3.3.1 Synthesis of g-$C_3N_4$

The preparation of graphitic carbon nitride with good photocatalytic property was very important. First by identifying the optimum process parameters which is temperature of 550 $^0$c in the preparation of graphitic carbon nitride (g-$C_3N_4$) and thermal condensation (pyrolysis) technique used for calcination of nitrogen rich precursor like urea put in furnace with aluminum covered crucible pyrolysis time of 240 min in order to get better surface area of the material, the observed yellowish color of the product confirms that the formation of g$C_3N_4$[28]. After cooled, the obtained product was used for further characterization and adsorptive-photocatalytic degradation of MB then analyze the synergistic effect of as prepared sample based on experimental variables and interaction carried out by application of Response Surface Methodology to model and optimize the process parameters.

### 3.3.2 Characterization

Various methods have been employed to characterize the physicochemical properties of graphitic carbon nitride (g-$C_3N_4$). The phase identification, the crystallinity of g-$C_3N_4$, and information on unit cell dimensions can be identified by (XRD)pattern which was scanned with x-ray char Cu Kα radiation (λ = 0.154059 nm) in scanning angle range of 10–60$^o$.The specific surface area distribution can be measured from nitrogen adsorption-desorption analysis using according to the Brunauer-Emmett-Teller (BET) method. The surface morphology of the prepared sample was investigated by scanning electron microscope (SEM). The surface functional group were obtained by the FTIR spectroscopy method. The commonly used region for absorption spectroscopy is 4000 ~ 400 $cm^{-1}$ because most organic compounds and inorganic ions absorption radiation are within this region. A UV-Vis spectrophotometer is used to scan spectra of the samples in the range of 200–800 nm. Photoluminescence (PL)also used to determine the electron hole pair recombination and transportation of charges.

### 3.3.3 Adsorption tests

For measurements of adsorption kinetics, 0.3 g of g-$C_3N_4$ (dosage of 3g/L) were added into each of experimental runs (17 runs) the 100 mL MB (5,10,15 mg/L) solutions to evaluate the effect of solution pH on the adsorption ability of g-$C_3N_4$, the mixture adjusted by HCl and NaOH at pH values of 4,7and 10. The suspensions were stirred in incubator shaker for 2 hours and 150 rpm speed. Samples then measured by UV–Vis spectrophotometer (X-ma 1200) at 664nm to determine the concentration. Select the optimum one then measured initial MB concentration and final concentration after adsorbent dose retention time of 2 hours with constant agitation to determine MB dye removal efficiency (Equation.1) and the adsorption capacity from fitted isotherm model in order to get the adsorption efficiency of the material.

### 3.3.4 Photodegradation test

The photocatalytic degradation was performed using an aqueous solution MB in 250 ml beaker under self-made visible light irradiation. The irradiation was carried out at the top of the beaker using 100 w visible light lamp (Panasonic). Process parameters such as solution pH, photocatalyst dose and adsorbate concentration with constant time and speed carried out according to the Box–Behnken Design (BBD) experimental design method as presented in table

3.1. In path of a complete MB molecule photocatalytic degradation there are four stages by which can undergo a complete photocatalytic degradation, (i) demethylation, (ii) ring shortening, (iii) ring opening and (iv) final oxidation or mineralization. According to literature[29]. the oxidation of methyl groups was performed by the hydroxyl radical, which gradually converts methyl groups to aldehyde, alcohol, carboxylic acid and ultimately decarboxylates to $CO_2$.

The photocatalytic degradation kinetics of g-$C_3N_4$ to MB solution at pH 4,7 and 10 were carried out in dark condition for 20 min that laid the adsorption /desorption interaction approaches the equilibrium then the lamp light was turn on immediately this made the photocatalytic reactions takes place because the active species produced by photo-induced carriers causes a continued degradation of the adsorbed reactant[30].The same as those of the adsorption experiments, the adsorption process and photocatalytic degradation process began at the same time. The MB concentrations then determined for 17 runs using a UV–Vis spectrophotometer (X-ma 1200) at 664 nm. After optimization measured the final TOC when illumination of light carried out then determine the efficiency of Photocatalysis process.

Table 3. 1 Experimental study factors and levels

| Factor | Name | Units | Minimum | Maximum |
|---|---|---|---|---|
| A | pH | | 4.00 | 10.00 |
| B | Adsorbent dose | g/l | 1.00 | 3.00 |
| C | Adsorbate concentration | mg/l | 5.00 | 15.00 |

During the photodegradation tests, known amount of catalyst dose and MB concentration continuously stirred with magnetic stirrer to make homogeneous conditions. Prior to each test, the mixture kept in dark condition to ensure equilibrium adsorption. After 20 min irradiation time, about 5 mL of the solution was withdrawn and filtered by syringe filter. Then, measured MB concentration using UV-Visible spectrophotometer (X-ma 1200 spectrophotometer) at an absorbance of 640nm. The optimum adsorbent dosage, volume of solution, and concentration change of MB were used to determined photocatalytic and adsorption efficiency (E) and adsorption capacity (qt) at a given time t using the following equations:

$$E\% = \frac{Ci - Cf}{Ci} * 100 \quad (1)$$

$$qt(mg/g) = \frac{Ci - Cf}{m} * V \quad (2)$$

where, Ci and Cf are the concentrations of MB at the initial and final irradiation time, m is mass of adsorbent in (g) and V the volume of solution respectively.

### 3.3.5 MB analysis using UV-visible spectrophotometer

Different MB solutions were measured using UV spectrophotometer (X-ma 1200 Spectrometer) at 640nm. An absorbance calibration curve was developed using different MB concentration as shown in Table 3.2 from 1 to 10 mg/l. The calibration curve (Appendix II) was constructed by plotting MB concentration versus absorbance which were used in reading off the unknown concentrations. The absorbance of samples was converted to MB concentration using the calibration curve equation developed in the equation of (y = mx + b) the value for the intercept (b), slope(m), absorbance (y), and concentration (x). slope passing through the origin, and y-intercept (b) zero is given by:

$$Slope(m) = \frac{y\ (Adsorbance)}{x\ (Concentration)} \quad (3)$$

Table 3. 2 Standard solutions and measured absorbance for calibration curve.

| Concentration(mg/L) | Absorbance |
|---|---|
| 0 | 0 |
| 1 | 0.003 |
| 2 | 0.01 |
| 4 | 0.015 |
| 6 | 0.028 |
| 8 | 0.037 |
| 10 | 0.054 |

### 3.4 Determination of adsorption isotherm model (Langmuir and Freundlich)

Equilibrium data, commonly known as adsorption isotherms, describe how the adsorbate interacts with adsorbents, and give a comprehensive understanding of the nature of the interaction. It is important to optimize the design of an adsorption system.

#### 3.4.1 Langmuir Adsorption isotherm

The theoretical Langmuir isotherm is valid for adsorption of a solute from a liquid solution as monolayer adsorption on a surface containing a finite number of identical sites[31]. The model assumes uniform energies of adsorption onto the adsorbent surface. The Langmuir non-linear equation is commonly expressed as:

$$\boldsymbol{q_e = \frac{q_m K_a C_e}{1 + K_a C_e}} \tag{4}$$

$C_o$ and Ce are the initial and equilibrium concentration of adsorbate respectively; V= value of pollutant solution (in liter); w = weight of adsorbent. $\boldsymbol{q_e}$ is a constant and reflects a complete monolayer ($mgg^{-1}$); $K_a$ is the adsorption equilibrium constant ($Lmg^{-1}$) that is related to the apparent energy of sorption. The Langmuir isotherm Eq. (4) can be linearized into the following form. A plot of $\frac{\boldsymbol{C_e}}{\boldsymbol{q_e}}$ versus $\boldsymbol{C_e}$ would be linear.

$$\boldsymbol{\frac{C_e}{q_e} = \frac{1}{K_a Q_m} + \frac{1}{Q_m} C_e} \tag{5}$$

$$\mathbf{RL} = \frac{\mathbf{1}}{\mathbf{1} + \boldsymbol{K_a C_o}} \tag{6}$$

The separation factor ($R_L$) as shown in Eq.6 is a constant in order to express the important characteristics of the Langmuir isotherm. The value of $R_L$ indicate the adsorption to be linear, favorable and unfavorable, also irreversible when $R_L$=1,0<$R_L$<1, $R_L$>1, and $R_L$=0, respectively [32].

### 3.4.2 The Freundlich isotherm

The Freundlich isotherm model (Freundlich, 1906) is the earliest known equation describing the adsorption process. It is an empirical equation and can be used for non-ideal sorption that involves heterogeneous adsorption. It is given by the following nonlinear equation below:

$$\boldsymbol{q_e = K_F C_e^{\frac{1}{n}}} \text{qe=}K_F C_e 1n \tag{7}$$

where $K_F$ is a constant for the system, related to the bonding energy. $K_F$ can be defined as the adsorption or distribution coefficient and represents the quantity of pollutant adsorbed onto adsorbent for unit equilibrium concentration. 1/*n* is indicating the adsorption intensity of pollutant onto the adsorbent or surface heterogeneity, becoming more heterogeneous as its value gets closer to zero. A value for 1/*n* below 1 indicates a normal Langmuir isotherm while 1/*n* above 1 is indicative of cooperative adsorption. Eq. (7) can be linearized in the logarithmic form and the Freundlich constants can be determined:

$$\mathbf{\log} \boldsymbol{q_e} = \mathbf{\log} \boldsymbol{K_F} + \frac{\mathbf{1}}{\boldsymbol{n}} \mathbf{\log} \boldsymbol{C_e} \tag{8}$$

A plot of $\mathbf{\log} \boldsymbol{q_e}$ versus $\mathbf{\log} \boldsymbol{C_e}$ would be linear.

### 3.5 Determination of photocatalytic kinetics (First and Second Order)

#### 3.5.1Lagergren pseudo-first-order equation

The photodegradation kinetics of MB at different time intervals can be analyzed by the Lagergren pseudo-first-order equation as depicted in Eq (9).

$$\mathbf{log(q_e - q_t) = log\, q_e - \frac{k_1 t}{2.303}} \quad (9)$$

Where: $q_e$ and $q_t$ = the amounts of MB adsorbed (mg $g^{-1}$) at equilibrium and at time t (min), respectively, $k_1$ ($min^{-1}$) is the adsorption rate constant. Based on experimental results, linear plots of log (qe-qt) versus $\boldsymbol{q_e}$ is tested the applicability of the Lagergren first-order equation to the adsorption of MB. The rate constant was calculated from the slope. The effect of MB concentration on rate constants ($k_1$) helps to describe the mechanism of degradation of MB from an aqueous solution.

#### 3.5.2The pseudo-second-order equation

The pseudo-second-order photodegradation kinetic rate equation [33] is expressed as;

$$\mathbf{\frac{dq_t}{dt} = k_2(q_e - q_t)^2} \quad (10)$$

where $k_2$ is the rate constant of pseudo-second-order adsorption ($g \cdot mg^{-1} \cdot min^{-1}$). For the boundary conditions t = 0 to t = t and qt = 0 to $q_t = q_t$, the integrated form of Eq. (10) becomes:

$$\mathbf{\frac{1}{(q_e - q_t)} = \frac{1}{q_e} + kt} \quad (11)$$

In which the integrated rate law for a pseudo-second-order reaction. Eq. (11) can be rearranged to obtain Eq. (12), which has a linear form:

$$\mathbf{\left(\frac{t}{q_t}\right) = \frac{1}{k_2 q_e^2} + \frac{1}{q_e}(t)} \quad (12)$$

if the initial adsorption rate, *h* ($mg \cdot g^{-1} \cdot min^{-1}$) is:

$$\mathbf{h = k_2 q_e^2} \quad (13)$$

then Eq. 14become:

$$\left(\frac{\mathbf{t}}{\mathbf{q_t}}\right) = \frac{\mathbf{1}}{\mathbf{h}} + \frac{\mathbf{1}}{\mathbf{q_e}}(\mathbf{t}) \quad (14)$$

The plot of ($t/q_t$) versus t could give a linear relationship from which $q_e$ and $k_2$ were determined from the slope and intercept of the plot, respectively.

### 3.5.3 Intraparticle diffusion model

The intraparticle diffusion model is expressed as follows;[30]

$$\mathbf{q_t = K_d t^{1/2} + C} \quad (15)$$

Where $k_d$ is the intraparticle diffusion rate constant (mg/g $min^{1/2}$), C is the intercept (mg /g). A plot of $q_t$ versus $t^{1/2}$ gives a linear relationship, from which the $k_d$ value was determined from the slope. The intercept of the plot reflects the boundary layer effect. If the regression of the plot is linear and passes through the origin, then intraparticle diffusion is the sole rate-limiting step.

### 3.6 Experimental Design and procedure

The synthesis of g-$C_3N_4$ and characterization using Uv-vis spectrophotometer, XRD, FTIR were done at AAU. Sample morphology characterized by scanning electron microscopy (SEM), nitrogen adsorption-desorption isotherm analysis using BET method for the surface area determination and PL analysis for recombination of electron hole pair by photogenerated charge carriers were characterized in AASTU and ASTU. The effect of pH, dose of adsorbent and concentration of dye were examined and the interaction between the variables or different reaction parameters and responses were established. Finally, the percentage of degradation was determined using DOE software and set up of self -made visible light bulb at same stirring rate with constant time obtained what initial concentration of methylene blue, adsorbate dose and how much contact time was required to adsorb the goal of achieving maximum percentage degradation of dye. Photocatalysis or Degradation process, RSM method based on Box-Behnken design was applied. As key factor variables Adsorbent dose, pH, Adsorbate concentration were used to analyze the influence of such different parameters. The experimental levels of

independent process variables involved in the adsorptive and photocatalysis process were given in Table 3.1.

For photocatalysis kinetics,0.3 g of g-$C_3N_4$ (dosage of 3g/L) were dispersed in to each of 100 mL of 5 mg/L MB solutions. The suspension was magnetically stirred at constant stirring rate in the dark for 20 minutes in order to reach at equilibrium and then placed self - made visible light irradiation set up for retention time of 2 hours and pH was adjusted respectively to evaluate the effect of solution pH on the photocatalysis efficiency, then 2 mL solution collected every 20 minutes to determine the concentration of MB by Uv-VIS spectrophotometer. After optimization measure TOC for both adsorption and photocatalysis efficiency determination.

## 4. Result and Discussion

### 4.1 Synthesis mechanism

After identifying the optimum process parameters which is temperature of 550 $^{0}$c in the preparation of graphitic carbon nitride (g-$C_3N_4$) through long-time thermally treating bulk g-$C_3N_4$ under an air atmosphere (a weak oxidizing atmosphere)[34]suggesting that higher temperature favors the nucleation and growth of g-$C_3N_4$. As a result, observed yellowish color of the product confirms that the formation of g$C_3N_4$.

### 4.2 Characterization of g-$C_3N_4$

#### 4.2.1 Crystallinity and phase identification

The XRD analysis in Figure 4.1 shows patterns of g-$C_3N_4$ (100) plane peak is observed 2Ɵ of 13.5$^{o}$ and the other major peak at 26.92$^{o}$(002) plane observed in graphitic carbons temperature of 550$^{o}$c and four hours pyrolysis time. The miner peaks 44.05$^{o}$, 45.98$^{o}$ (103) and 54.56$^{o}$(004) and the width 2.45 minor and 3.205 major of the peak provides information about the materials structure[35]. According to Scherrer equation, the crystal size of g-$C_3N_4$ was computed by formula $D = K\lambda/\beta\cos\theta$, where D is the crystallite size (nm), K the Scherrer constant (about 0.9), λ the wavelength of Cu-Kα radiation (0.15418nm), and β the full width of (002) diffraction peak at half maximum. The average crystallite size was found to be 2.7 nm. when the pyrolysis time is prolonged implies that the diffraction peak intensity becomes stronger and observed perfect graphite. This increase in peak intensity 550 $^{o}$C with prolonged pyrolysis time 4hrs indicates that the crystallinity of g-$C_3N_4$ is improved.

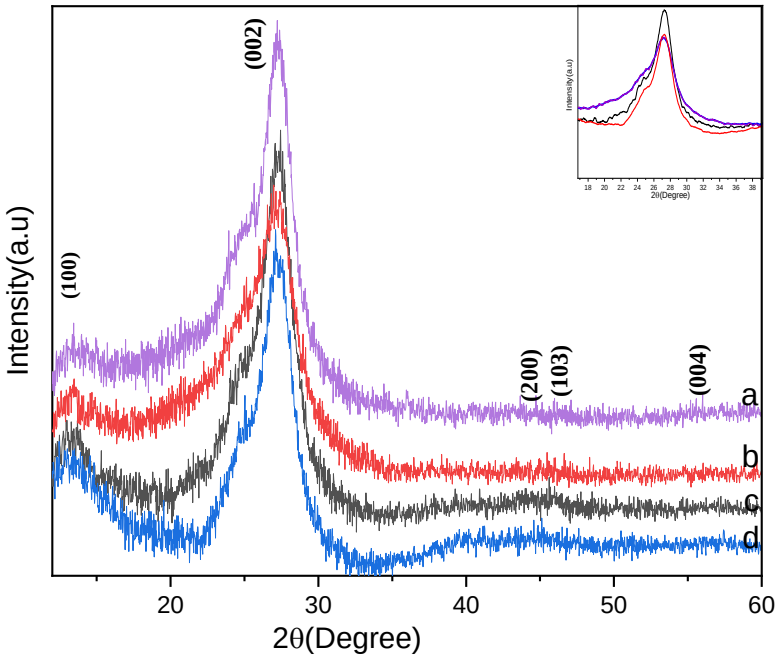


Figure 4. 1 XRD pattern of g-$C_3N_4$ for different temperature and pyrolysis time 500 $^oC$-3 hrs (a), 550 $^oC$-3 hrs (b), 550 $^oC$-4 hrs (c), 500 $^oC$-4 hrs (d)

### 4.2.2 FTIR analysis

FTIR spectra of four g-$C_3N_4$ samples exhibited a broad-peak ranging from 3000 to 3500 $cm^{-1}$ corresponding to the signatures of the absorbed water molecule and N-H vibration of the free amino groups and adsorbed hydroxyl species, respectively. Also, the strong bands observed in the range of 1200–1650 $cm^{-1}$ confirmed that for success fully prepared g-$C_3N_4$ and C-N heterocycles as either C-NH-C or C-N(-C)-C units. Infrared-active mode situated at 1640 $cm^{-1}$ is due to C-N stretching, while at 1555, 1460 and 1408 $cm^{-1}$, corresponding to the typical stretching vibration modes of C-N heterocycles. On the other hand, the bands observed at about 1324 and 1248 $cm^{-1}$ stretching vibration of the connected units of C-NH-C (Figure 4.2). The sharp peak absorption band at 808 $cm^{-1}$ corresponds to breathing vibration mode of the triazine group, the absorption band at 888 $cm^{-1}$ assigning to deformation mode of N–H[7].

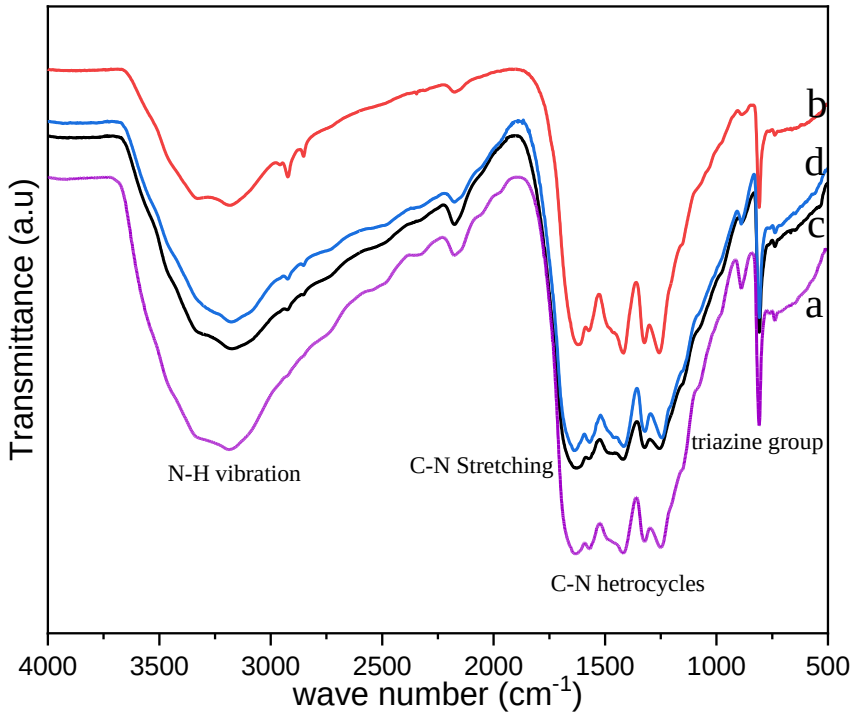


Figure 4. 2 FTIR (Fourier transform infrared spectrophotometer) spectra of four g-$C_3N_4$ as prepared samples

### 4.2.3 SEM analysis

SEM images described in Figure 4.3 are the morphology of as-prepared four samples of g-$C_3N_4$ in the magnitude of 200 µm, in order to analyze particle size by using length or line tool on image j obtained better result at 550 $^oC$ 4 hours pyrolysis time. the grain morphology and the average particle size can be estimated by this analysis. As can be seen below grain clusters stacked disorderly that result caused by gas bubbles during pyrolysis of urea interconnected with thin layers[36].

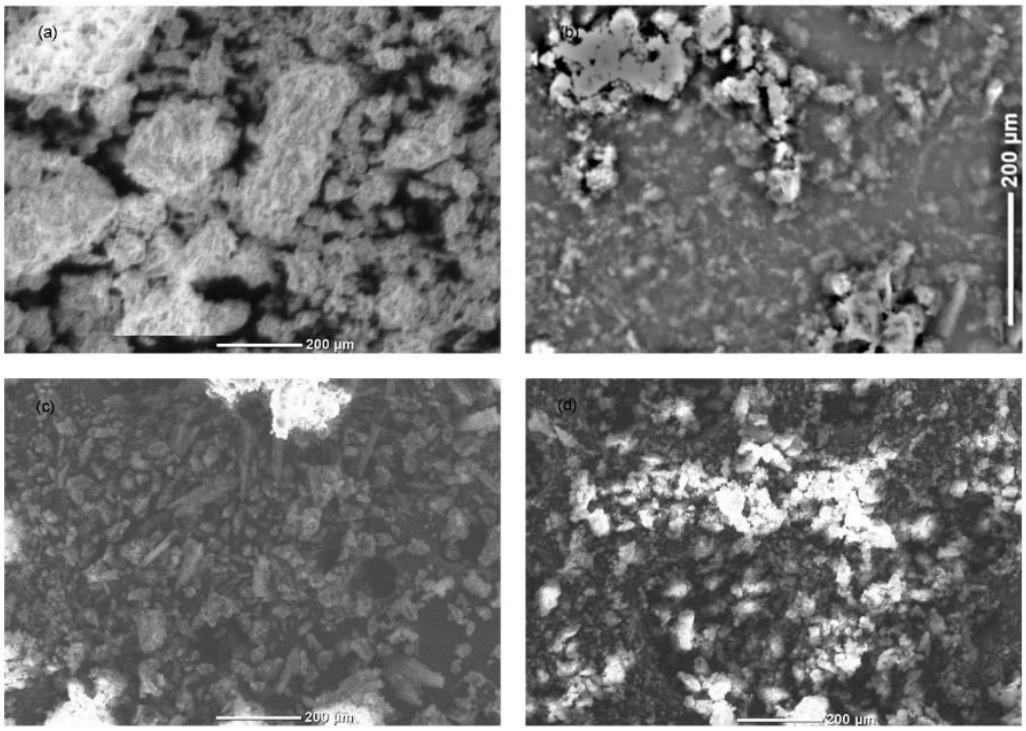


**Figure 4. 3 SEM images with the same magnification for 500 °c-3hrs(a), 550 °c-3hrs (b), 550 °c-4hrs (c), 500 °c-4hrs (d)**

### 4.2.4 BET

Nitrogen adsorption–desorption measurements were to examine the specific surface area as shown in Appendix I, the maximum surface area was determined at 550 °C pyrolysis time of four hours to be 54.9 $m^2/g$ in the relative pressure range of $0.5 < P/Po < 0.1$. In order to get the higher BET surface area and larger pore size distribution should create the effective prevention of the aggregation of the g-$C_3N_4$ by the self-producing atmosphere (inert atmosphere by applying nitrogen gas). The large surface area and pore volume can provide more reactive sites and more edge structures and may effectively adsorb more reactants and be conducive to mass transfer and charge carrier transfer during the photocatalytic process[36].

### 4.2.5 PL analysis

Photoluminescence (PL) spectroscopy was performed to determine the recombination of electron-hole pair, separation and migration of photogenerated charge carriers. As shown in Figure 4.4 g-$C_3N_4$ had broad peak centered at 424nm best PL results at 550 °C pyrolysis time of 4 hours that showed emissions of light in the range of visible light.

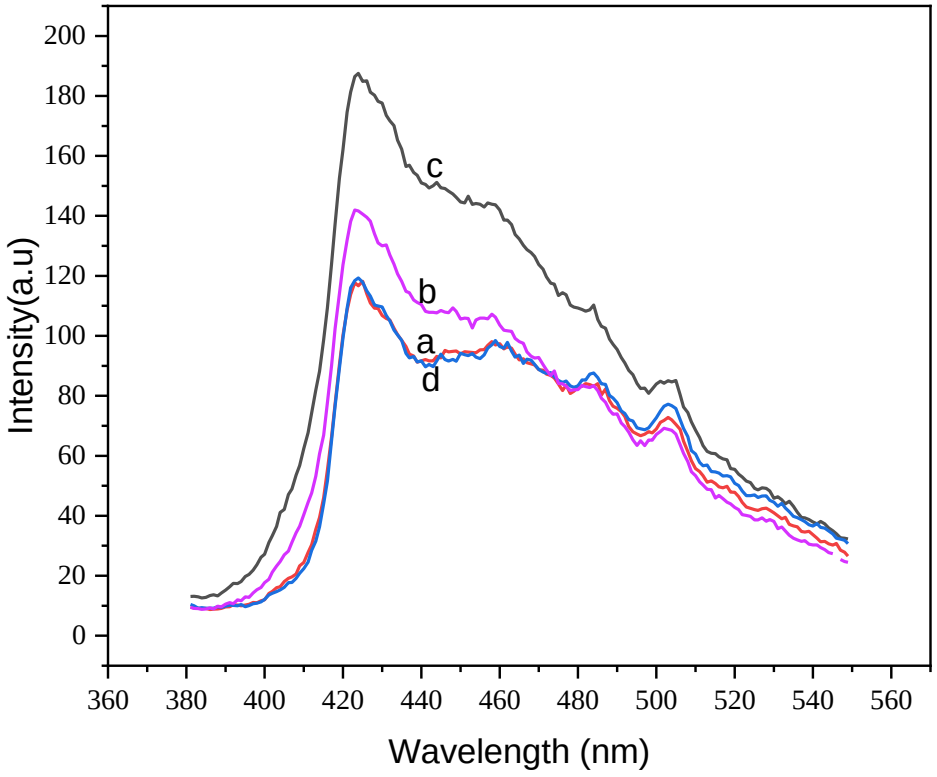


Figure 4. 4 PL spectra of g-$C_3N_4$ samples treated for 500 $^{o}$c-3hrs(a), 550 $^{o}$c-3hrs (b), 550 $^{o}$c-4hrs (c), 500 $^{o}$c-4hrs (d)

### 4.3 Photocatalytic performance

#### 4.3.3 Effect of reaction parameters

Interaction effect of pH, adsorbent dose and adsorbate concentration on Photocatalysis efficiency are discussed in this section. Figure shows the response Photocatalysis efficiency as a function of pH and adsorbent dose under experimental conditions. From figure 4.5, it can be seen that higher percentage occurred at 7-10 pH and at maximum dose. The contact time of 2 hours, concentration of adsorbate 5ppm and pH of 7 indicates photocatalysis efficiency (96%) as shown in figure 4.7.

#### 4.3.4 Effect of pH

0.1 M NaOH and 0.1 M HCl were used to adjust the solution pH of the experiments. Standard Sodium Hydroxide (0.100 N) was prepared by adding 2 g of sodium Hydroxide in 500 mL of volumetric flask, filled distilled water to the mark and M (35.4%) of Hydrochloric Acid (HCl) adding 4.36 mL in 500 mL of volumetric flask put water until reached to the mark.

The initial concentration of MB was adjusted with 0.1 M $H_2SO4$ and 0.1 M NaOH then different amount of dose was added to the prepared dye solution of desired pH value. The pH of the initial dye solution was maintained at 4, 7, and 10. The samples were then stirred with magnetic stirrer for determination of photocatalysis process.

The rate of photodegradation caused by g-$C_3N_4$ is poor in lower pH and showed best performance within the neutral pH values of 7-8 and degradation started to become decreased at basic pH values. Such pH dependency of the photocatalytic reactions caused by catalyst surface may be positively or negatively charged due to the surface adsorption of $H^+$ or $OH^-$ ions, respectively and coulombic interactions between the catalyst and MB[37]. Therefore, at lower or higher solution pH, coulombic repulsions force between the similarly charged photocatalyst and MB molecule prevents interaction and charge transfer rate between two species also due to MB is a cationic reactive dye which can deposition on negatively charged surface due to electrostatic attraction. As highly reactive hydroxyl radicals are generated only at the contact point of the photocatalyst and water, if it cannot reach the MB molecule and hence the overall rate of photocatalytic degradation of MB decreases.

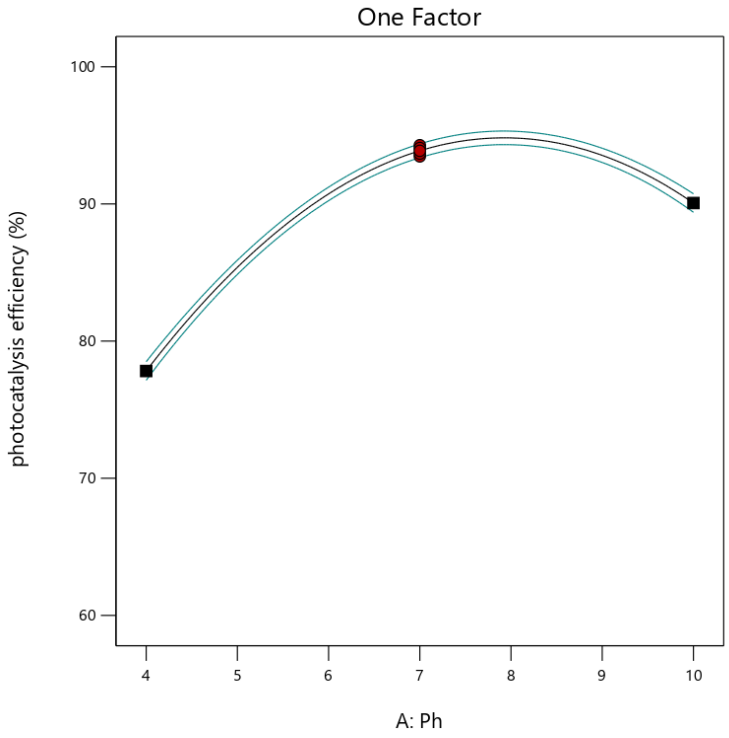


Figure 4. 5 Effect of pH on photocatalysis efficiency

### 4.3.5 Effect of adsorbent Dosage

The effect of adsorbent dosage was determined by vary the amount of adsorbent from 1g to 3g/lt. A known amount of catalyst was added to 100ml of different MB concentrations in 250 plastic flasks then stirred with magnetic stirrer for determination of photocatalysis process. The result verified by increasing adsorbent dose optimize degradation efficiency of the material and organic pollutant in water which was because of providing more active sites.

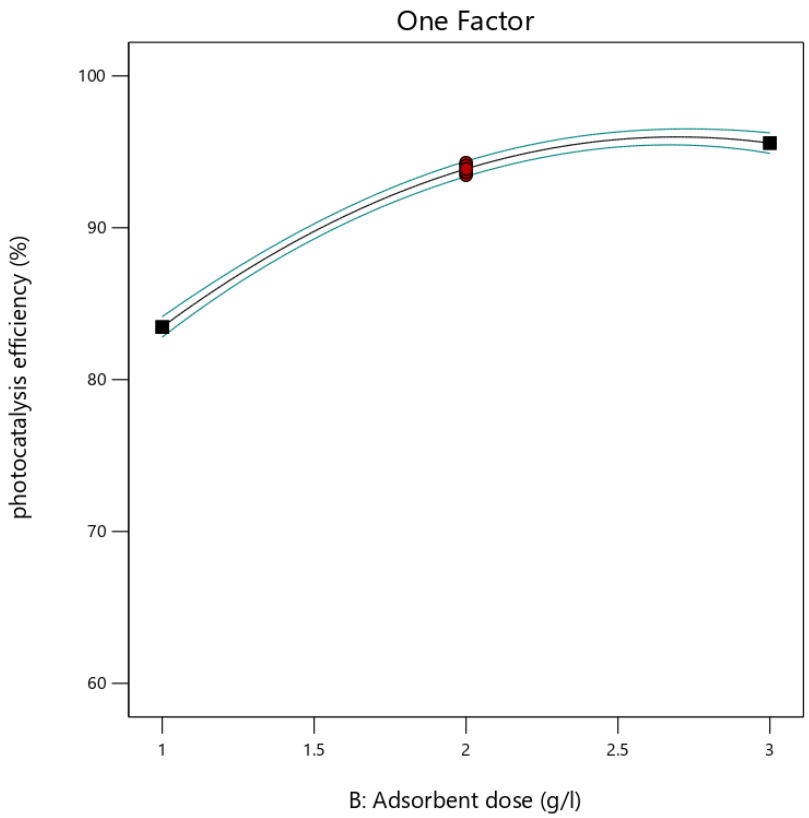


Figure 4. 6 Effect of Adsorbent dose on photocatalysis efficiency

### 4.3.6 Effect of adsorbate concentration

The effect of adsorbate concentration was determined by varying the concentration of MB from 5ppm to 15 ppm. 100ml of such different concentrations mixed with different adsorbent dose in 250 plastic Flask. The samples were then stirred with magnetic stirrer for determination of photocatalysis process and using shaker for determination of adsorption efficiency. As shown from figure 4.7 the degradation efficiency was higher at initial concentration of MB which was due to the limited active sites and limited hydroxyl radicals generated during photocatalysis reaction[37].After optimization result of experimental works in lab based on the optimum operating parameters of the solution pH of 7.26, initial adsorbate concentration of 5.08 mg/L, and the adsorbent dose of 2.52 g/L with desirability of 1 as shown in fig 4.11 predicated by the model were 51 % adsorption efficiency(Co of 8.77mg/L, Cf of 4.29 mg/L) and 96.02% of photocatalysis efficiency.

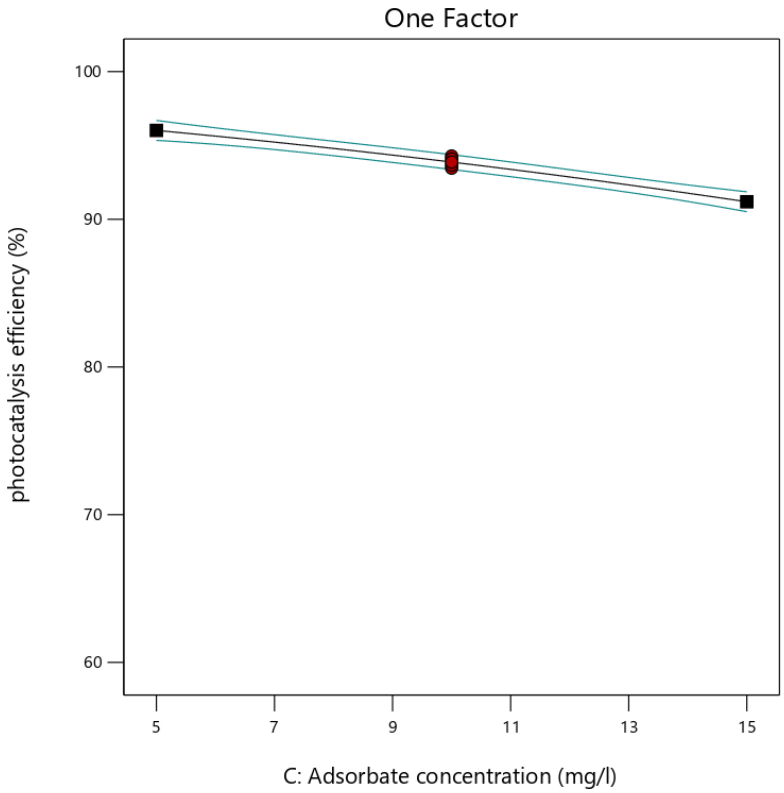


Figure 4. 7 of Adsorbate concentration on photocatalysis efficiency

### 4.3.7 Interaction effects dose of photocatalyst and initial methylene blue concentration

The influence of two reaction parameters shown in figure 4.8 that rate of degradation is faster for higher dose of photocatalyst because of provided more active sites and number of electron-hole pairs under visible light giving rise to larger amount of hydroxyl radicals, which increases rate of photodegradation of MB.

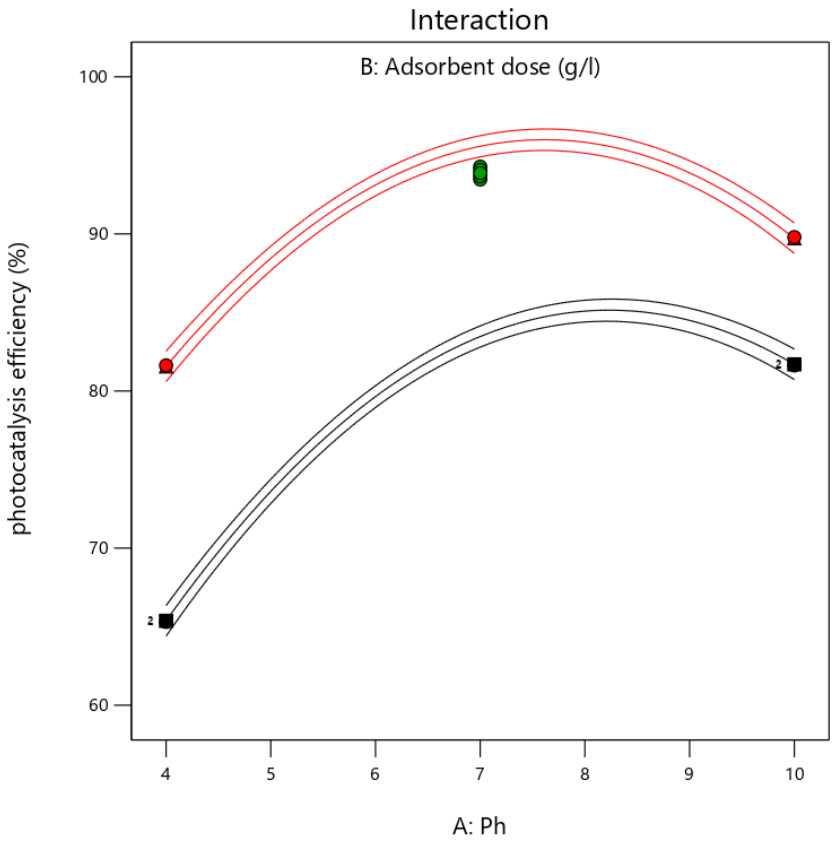


Figure 4. 8 Interaction effects dose of photocatalyst and initial methylene blue concentration

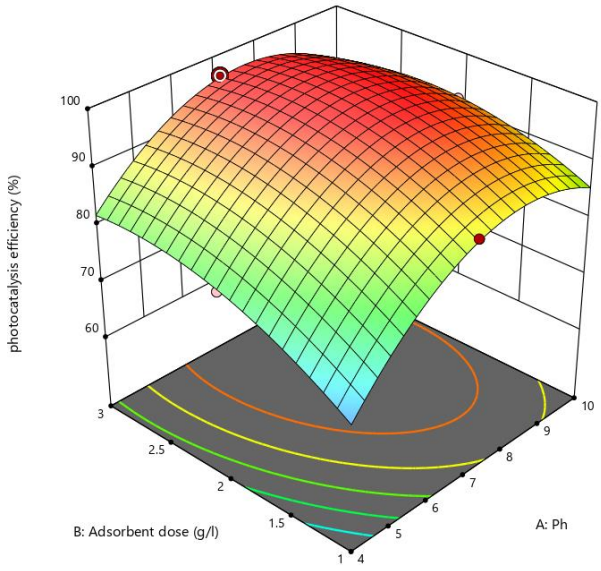
photocatalysis efficiency (%)
100
90
80
70
60
3
2.5
2
1.5
1
B: Adsorbent dose (g/l)
4
5
6
7
8
9
10
A: Ph

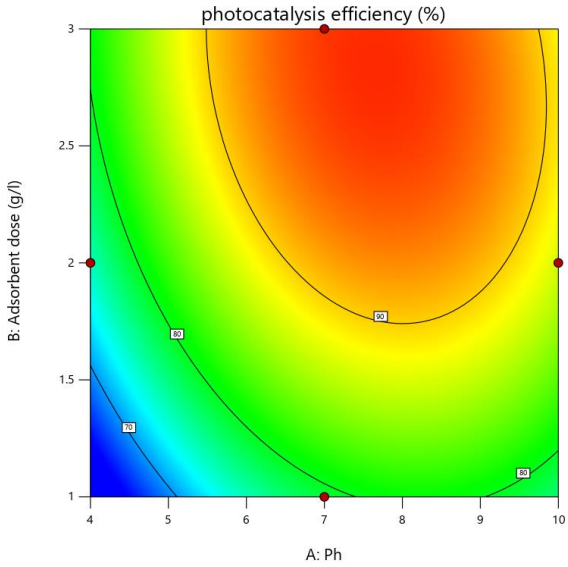
photocatalysis efficiency (%)
B: Adsorbent dose (g/l)
3
2.5
2
1.5
1
80
90
70
80
4
5
6
7
8
9
10
A: Ph

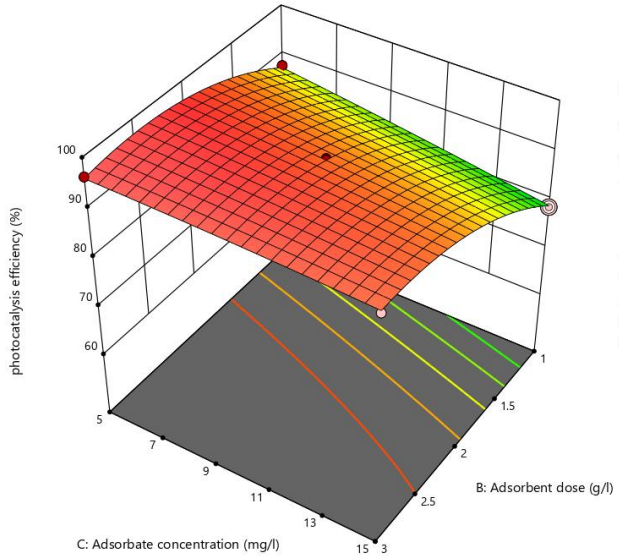
photocatalysis efficiency (%)
100
90
80
70
60
5
7
9
11
13
15
C: Adsorbate concentration (mg/l)
1
1.5
2
2.5
3
B: Adsorbent dose (g/l)

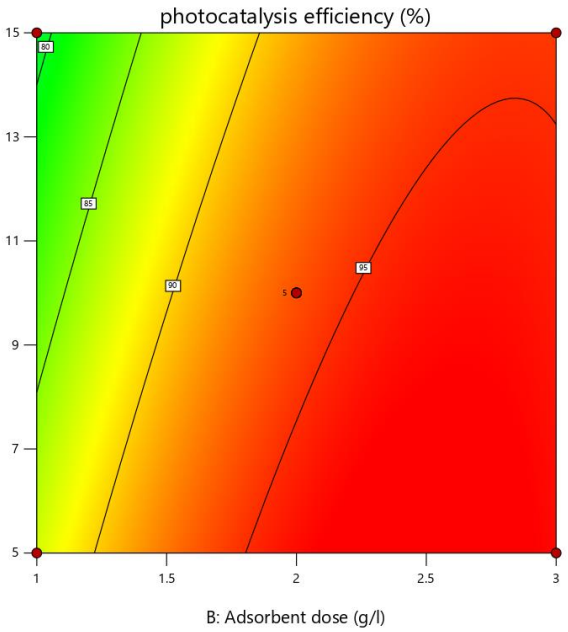
photocatalysis efficiency (%)
C: Adsorbate concentration (mg/l)
15
13
11
9
7
5
80
85
90
95
5
1
1.5
2
2.5
3
B: Adsorbent dose (g/l)

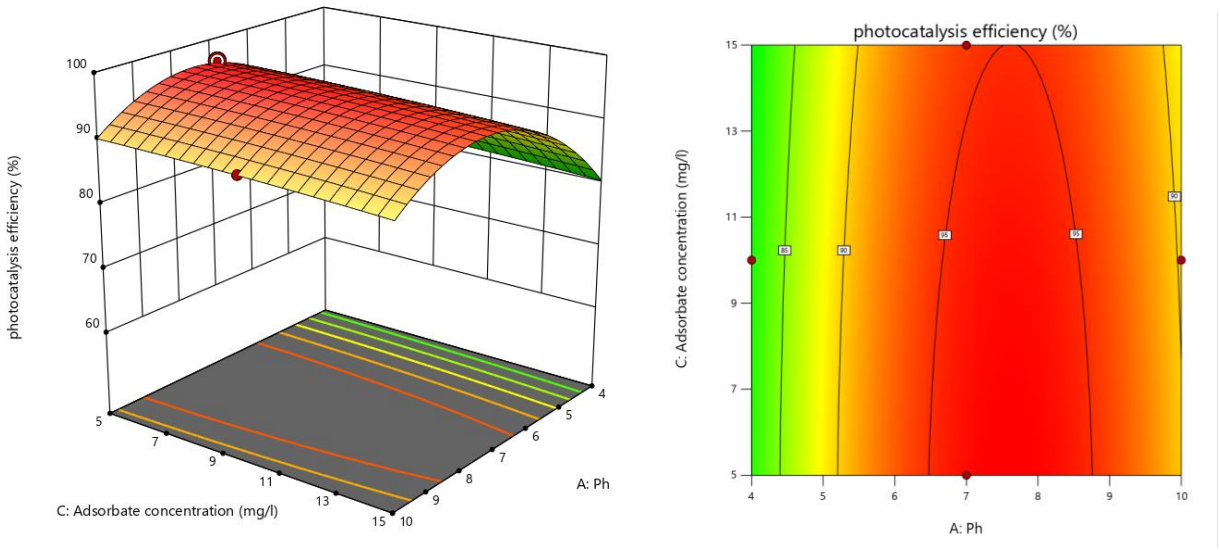


Figure 4. 9 3D surface plot of MB degradation as a function of (a) solution pH and Adsorbent dose, (b) Adsorbate concentration and Adsorbent dose, (c) solution pH and Adsorbate concentration and its contour respectively.

### 4.3.8 Analysis of variance

The experiments were designed according to Response surface methodology (RSM) which is an empirical modeling approach used to determining the correlation between the operational variables and response also distinguish the factors that affect the response function. As shown in table4.6 the analysis of variance (ANOVA) correlates the parameters with the responses (photocatalytic efficiency) were found significant with F-value of 587.54 and P value less than 0.05 indicate model terms are significant, whereas values greater than 0.1000 indicate the quadratic equation model terms are not significant. Accordingly, for photocatalytic efficiency the model terms A, B, C, AB, BC, $A^2$ and $B^2$, were found to be significant, the F and the p values of lack of fit were found 3.70 and 0.1191 that implies the "lack of fit" was not significant and indicates that the model equations are good for predicting the photocatalytic efficiency of the as prepared sample. There were 11.9% chances that "lack of fit F-values" such large value could occur due to noise.

### 4.3.9 Model fit summary

The sequential model fittings presented in table 4.2 and table 4.3 show that quadratic model was suggested for the analysis of experimental response. From the lack of fit tests, insignificant lack of fit was desirable for a model to fit the given experimental data. For the regression model of photocatalytic efficiency as shown in table 4.4 was 0. 9987. Which implies that the model described for 99.87% variability within the experimental range. Furthermore, the "pred $R^2$" values of 0.9839 were in reasonable agreement with the "Adj $R^2$" of 0.9970 because of the difference was less than 0.2. In general, for a good model, $R^2$ and prediction $R^2$ values should be close to 1 the "adeq Precision" was 84.28 which measure the signal to noise ratio and it is always desired to be greater than 4 that noise is very low. In conclusion, the suggested quadratic model can be used to navigate the design space with good accuracy. The model predicted values and the actual experimental values were compared in Table 4.7.

### 4.3.10 Diagnostic plots

The model adequacy was further checked by drawing different diagnostic plots in order to find out whether the model equations sufficiently approximate to the actual values or not. Figure 4.11 shows that the normal % probability plot of residuals for the responses are normally distributed, indicate that the actual values lie relatively near to the straight line.

Table 4. 1 Table Experimental runs arranged according to BBD-RSM

| | | Factor 1 | Factor 2 | Factor 3 | Response 1 |
|---|---|---|---|---|---|
| Std | Run | A: pH | B: Adsorbent dose | C: Adsorbate concentration | photocatalysis efficiency |
| | | | g/l | mg/l | % |
| 14 | 1 | 7 | 2 | 10 | 93.4694 |
| 17 | 2 | 7 | 2 | 10 | 93.8776 |
| 8 | 3 | 10 | 2 | 15 | 87.7551 |
| 4 | 4 | 10 | 3 | 10 | 89.7959 |
| 10 | 5 | 7 | 3 | 5 | 96.3265 |
| 5 | 6 | 4 | 2 | 5 | 79.5918 |
| 11 | 7 | 7 | 1 | 15 | 78.7755 |
| 15 | 8 | 7 | 2 | 10 | 94.0816 |
| 13 | 9 | 7 | 2 | 10 | 94.2857 |
| 9 | 10 | 7 | 1 | 5 | 87.7551 |
| 2 | 11 | 10 | 1 | 10 | 81.6327 |
| 3 | 12 | 4 | 3 | 10 | 81.6327 |
| 16 | 13 | 7 | 2 | 10 | 93.6735 |
| 12 | 14 | 7 | 3 | 15 | 94.1497 |
| 6 | 15 | 10 | 2 | 5 | 91.8367 |
| 7 | 16 | 4 | 2 | 15 | 75.5102 |
| 1 | 17 | 4 | 1 | 10 | 65.3061 |

Table 4. 2 Sequential model sum of squares

| Source | Sum of Squares | Df | Mean Square | F-value | p-value | |
|---|---|---|---|---|---|---|
| Mean vs Total | 1.288E+05 | 1 | 1.288E+05 | | | |
| Linear vs Mean | 639.78 | 3 | 213.26 | 5.04 | 0.0156 | |
| 2FI vs Linear | 28.23 | 3 | 9.41 | 0.1802 | 0.9074 | |
| Quadratic vs 2FI | 520.56 | 3 | 173.52 | 771.97 | < 0.0001 | Suggested |
| Cubic vs Quadratic | 1.16 | 3 | 0.3856 | 3.70 | 0.1191 | Aliased |
| Residual | 0.4165 | 4 | 0.1041 | | | |
| Total | 1.299E+05 | 17 | 7643.67 | | | |

Table 4. 3 Fit Summary for photocatalysis efficiency

| Source | Sequential p-value | Lack of Fit p-value | Adjusted $R^2$ | Predicted $R^2$ | |
|---|---|---|---|---|---|
| Linear | 0.0156 | < 0.0001 | 0.4309 | 0.2225 | |
| 2FI | 0.9074 | < 0.0001 | 0.2981 | -0.4622 | |
| Quadratic | < 0.0001 | 0.1191 | 0.9970 | 0.9839 | Suggested |
| Cubic | 0.1191 | | 0.9986 | | Aliased |

Table 4. 4 Table Fit Statistics of Photocatalysis Efficiency

| | | | |
|---|---|---|---|
| Std. Dev. | 0.4741 | $R^2$ | 0.9987 |
| Mean | 87.03 | Adjusted $R^2$ | 0.9970 |
| C.V. % | 0.5448 | Predicted $R^2$ | 0.9839 |
| | | Adeq Precision | 84.2808 |

Table 4. 5 experimental factors with their levels

| Factor | Name | Units | Minimum | Maximum |
|---|---|---|---|---|
| A | pH | | 4.00 | 10.00 |
| B | Adsorbent dose | g/l | 1.0000 | 3.00 |
| C | Adsorbate concentration | mg/l | 5.00 | 15.00 |

Table 4. 6 ANOVA Response Surface Quadratic Model for Photocatalytic efficiency

| Source | Sum of Squares | df | Mean Square | F-value | p-value | |
|---|---|---|---|---|---|---|
| Model | 1188.57 | 9 | 132.06 | 587.54 | < 0.0001 | Significant |
| A-pH | 299.88 | 1 | 299.88 | 1334.12 | < 0.0001 | |
| B-Adsorbent dose | 293.25 | 1 | 293.25 | 1304.64 | < 0.0001 | |
| C-Adsorbate concentration | 46.66 | 1 | 46.66 | 207.57 | < 0.0001 | |
| AB | 16.66 | 1 | 16.66 | 74.12 | < 0.0001 | |
| AC | 0.0000 | 1 | 0.0000 | 0.0000 | 1.0000 | |
| BC | 11.57 | 1 | 11.57 | 51.47 | 0.0002 | |
| $A^2$ | 415.34 | 1 | 415.34 | 1847.83 | < 0.0001 | |
| $B^2$ | 79.81 | 1 | 79.81 | 355.07 | < 0.0001 | |
| $C^2$ | 0.3118 | 1 | 0.3118 | 1.39 | 0.2774 | |
| Residual | 1.57 | 7 | 0.2248 | | | |
| Lack of Fit | 1.16 | 3 | 0.3856 | 3.70 | 0.1191 | not significant |

| | | | | | | |
|---|---|---|---|---|---|---|
| Pure Error | 0.4165 | 4 | 0.1041 | | | |
| Cor Total | 1190.14 | 16 | | | | |

Table 4. 7 Experimental runs according to BBD

| Run | A<br>pH | B<br>Adsorbent Dose (g/L) | C<br>Adsorbate concentration (mg/L) | Actual value | predicted value |
|---|---|---|---|---|---|
| 1 | 7 | 2 | 10 | 93.47 | 93.88 |
| 2 | 7 | 2 | 10 | 93.88 | 93.88 |
| 3 | 10 | 2 | 15 | 87.76 | 87.38 |
| 4 | 10 | 3 | 10 | 89.8 | 89.73 |
| 5 | 7 | 3 | 5 | 96.33 | 96.02 |
| 6 | 4 | 2 | 5 | 79.59 | 79.97 |
| 7 | 7 | 1 | 15 | 78.78 | 79.08 |
| 8 | 7 | 2 | 10 | 94.08 | 93.88 |
| 9 | 7 | 2 | 10 | 94.29 | 93.88 |
| 10 | 7 | 1 | 5 | 87.76 | 87.31 |
| 11 | 10 | 1 | 10 | 81.63 | 81.7 |
| 12 | 4 | 3 | 10 | 81.63 | 81.56 |
| 13 | 7 | 2 | 10 | 93.67 | 93.88 |
| 14 | 7 | 3 | 15 | 94.15 | 94.59 |
| 15 | 10 | 2 | 5 | 91.84 | 92.21 |
| 16 | 4 | 2 | 15 | 75.51 | 75.14 |
| 17 | 4 | 1 | 10 | 65.31 | 65.37 |

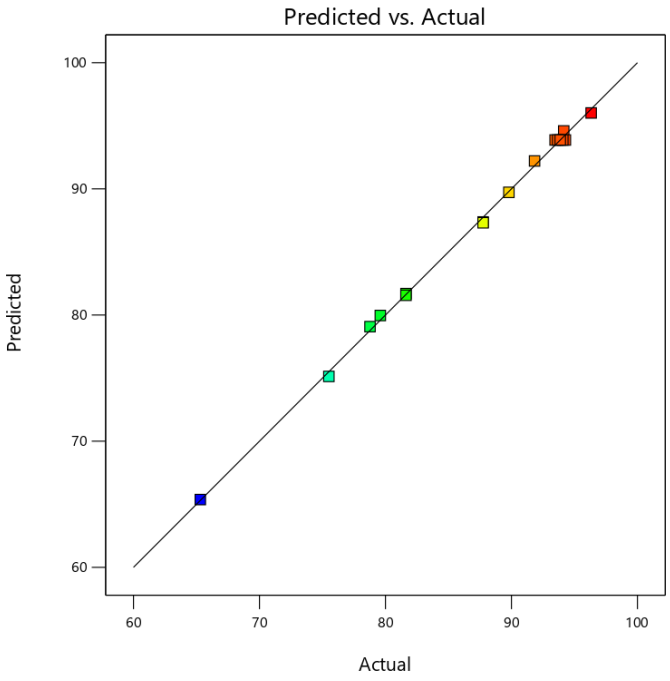


Figure 4. 10 predicted vs actual of the photocatalysis efficiency

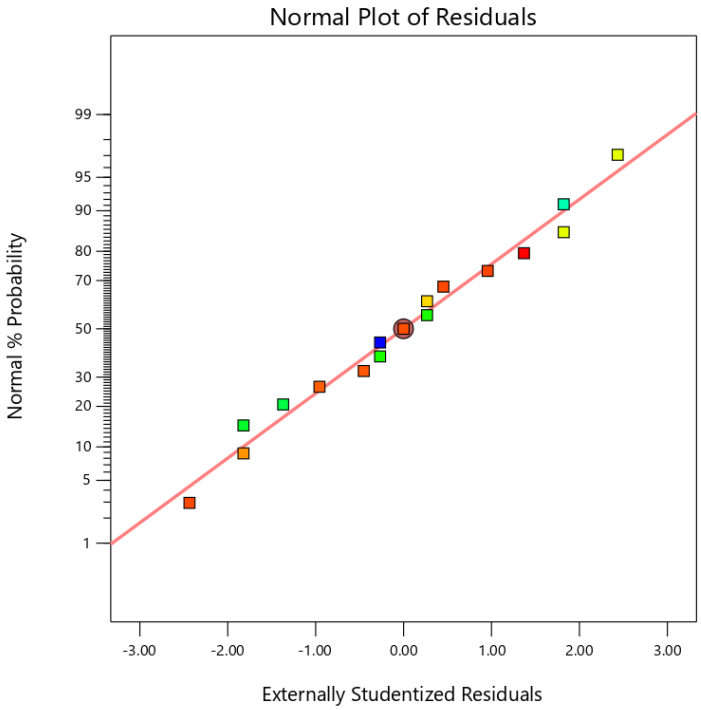


Figure 4. 11 Normal Probability of the photocatalysis efficiency

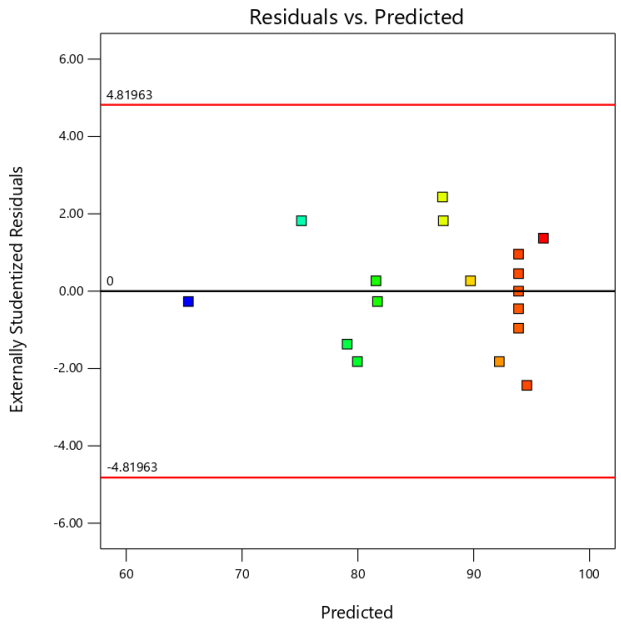


Figure 4. 12 Residuals vs Predicted plot of the photocatalysis efficiency

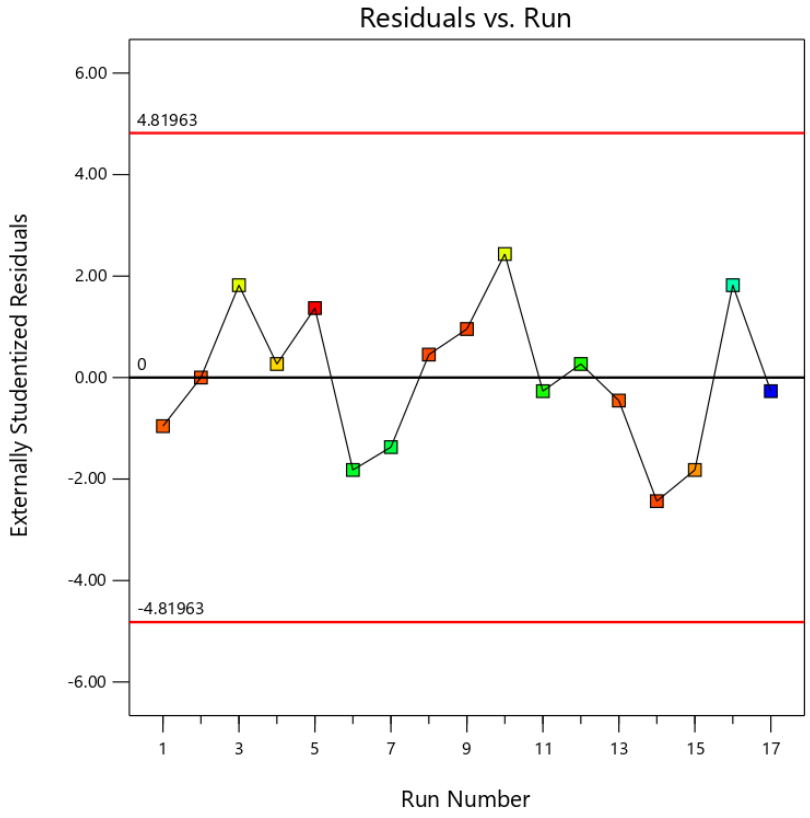


Figure 4. 13 Externally Studentized Residuals plot of the photocatalysis efficiency

### 4.4 Optimization Process

In synthesis process the furnace temperature and retention time were two vital parameters to improve the reactivity of precursors and diffusion processes. RSM was applied to model and optimize different parameters total of seventeen experimental runs and five center points were carried out. Experimental results were fed to design expert software for multiple regression fitting.

#### 4.4.1 Optimization of the process parameters and validation

The optimal condition to obtain maximum photocatalysis efficiency according to the Box–Behnken design, was calculated by Derringer's desired function methodology. The obtained optimum conditions were evaluated by composite desirability, which has values from 0 to 1, in order to determine to what degree, the optimum conditions satisfy the ultimate goal of response[38]. For optimization, the independent variables pH, adsorbent dose and adsorbate concentration were set within the studied level pH (4,7,10), adsorbent dose (1,2,3 g/L) and adsorbate concentration (5,10,15 mg/L) respectively. As a result of experimental works in lab based on the optimum operating parameters of the solution pH of 7.26, initial adsorbate concentration of 5.08 mg/L, and the adsorbent dose of 2.52 g/L with desirability of 1 as shown in Figure 4.14 predicated by the model were 96.32% and the optimum parameter confirmation was 96.02% photocatalysis efficiency, which is close to the optimization numerical solution. The optimum operational parameter of adsorption process in dark condition confirms that 51 % adsorption efficiency as shown (Appendix X). The final equation to make prediction about the response for level of each factor obtained in terms of actual factors was as follows.

$$\text{Photocatalysis efficiency (\%)} = 18.85A + 24.83B - 0.95C - 0.68AB - 1.74 * 10^{-15}AC + 0.34BC - 1.10A^2 - 4.35B^2 - 0.01C^2 - 2.99 \quad (17)$$

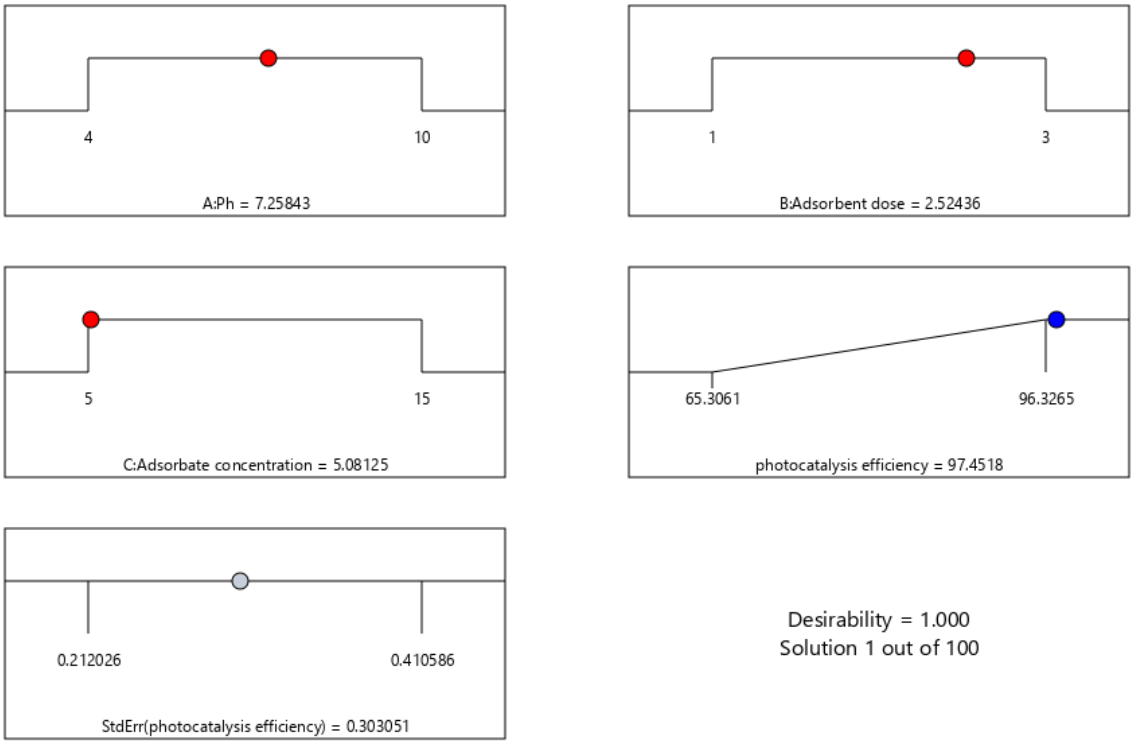


Figure 4. 14 Optimization numerical solution

### 4.5 Evaluation of the Langmuir and Freundlich Equilibrium adsorption isotherm model

The linear equilibrium adsorption data of MB g-$C_3N_4$ surface was analyzed using Langmuir and Freundlich model. The resulting plots were shown in Figure (4.15) which demonstrates correlation between Ce/qe and Ce, it represents linear correlation with $R^2$ of 0.95, that is higher than what was observed in the log qe and log Ce linear correlation with $R^2$ of 0.63 Freundlich model plot. The $R^2$ of the Langmuir model is higher than that of the Freundlich isotherm for the determination of adsorption of MB which means that the Langmuir adsorption isotherm more accurately described or represent the adsorption of MB on the surface of the material this expresses surface of the adsorbent is uniform and equal adsorption site only monolayer adsorption take place on the homogeneous surface of adsorbent. The values of $K_a$, $K_F$, qm, and n were determined from the slopes and intercepts of the two equations after plotting Ce/qe versus Ce and ln Ce versus ln qe. Similar results have been reported by other researchers in the study [41] as seen in Table 4.9, the maximum adsorption capacity (Q max) and adsorption constant of Langmuir model (Ka), for MB are 552 mg g−1 and 1.76 L mg−1, respectively. From the data calculated in table 4.8, the $R_L$ (0.102) was in between 0 and 1, that indicating Langmuir isotherm is favorable. The value of n=1 demonstrates that the equilibrium distribution between the solid and liquid phases is independent of concentration, while $\frac{1}{n} > 1$ indicates cooperative adsorption and $\frac{1}{n} < 1$ indicates normal adsorption [42].

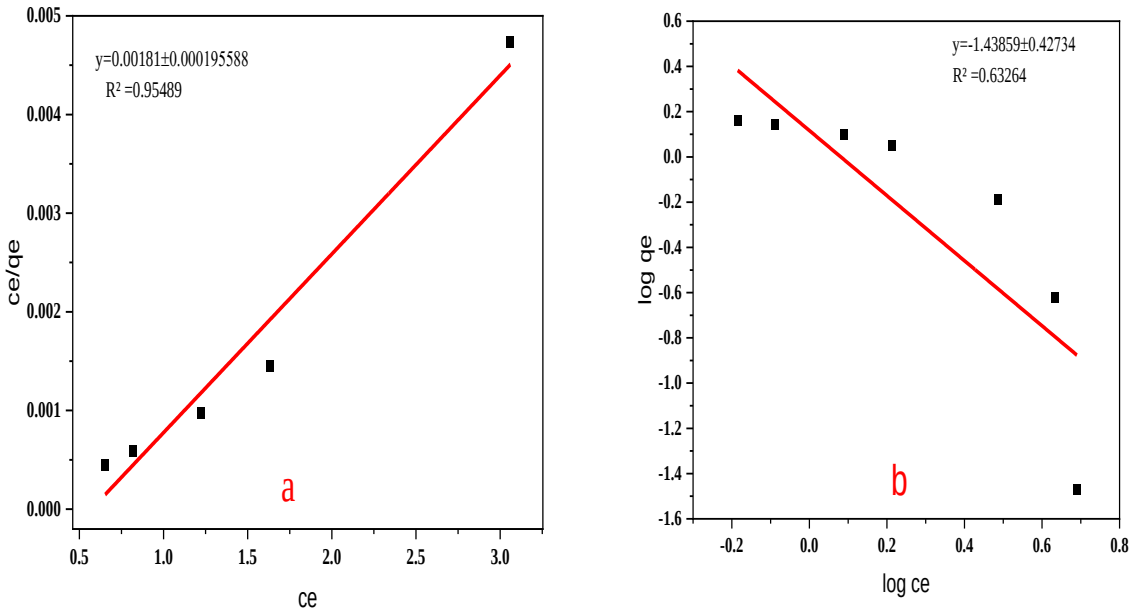


Figure 4. 15 Adsorption Isotherm models of (a) Langmuir and (b) Freundlich.

Table 4. 8 Experimental data for Langmuir and Freundlich Adsorption Isotherm model

| Time | Absorbance | Ce | Qe | log Ce | log qe |
|---|---|---|---|---|---|
| 0 | 0.024 | 4.897959184 | 0.034014 | 0.690015 | -1.46835 |
| 20 | 0.021 | 4.285714286 | 0.238095 | 0.632023 | -0.62325 |
| 40 | 0.015 | 3.06122449 | 0.646259 | 0.485895 | -0.18959 |
| 60 | 0.008 | 1.632653061 | 1.122449 | 0.212894 | 0.050167 |
| 80 | 0.006 | 1.224489796 | 1.258503 | 0.087955 | 0.099854 |
| 100 | 0.004 | 0.816326531 | 1.394558 | -0.08814 | 0.144437 |
| 120 | 0.0032 | 0.653061224 | 1.44898 | -0.18505 | 0.161062 |

Table 4. 9 The values of Langmuir and Freundlich constants

| Adsorption Isotherm models | Parameters | Concentration (5 mg/L) |
|---|---|---|
| Langmuir | Ka | 1.76 $Lmg^{-1}$ |
| | $q_m$ | 552 $mgg^{-1}$ |
| | $R_L$ | 0.102 |
| | $R^2$ | 0.955 |
| Freundlich | $K_F$ | 1.307 $Lmg^{-1}$ |
| | N | 0.695 |
| | $R^2$ | 0.633 |

## 4.6 Kinetic Study

### Adsorption and photocatalytic degradation kinetics

To determine the efficiency and interaction of the two processes in contaminants removal, the adsorption and photocatalytic degradation kinetics of MB removal by g-$C_3N_4$ at pH = 7 were first investigated. Due to the surface degradation or photodegradation process, the first-order model described the experimental data very well with $R^2$ of 0.962 (Appendix VI). For the convenience of comparison, other models also shown below the commonly used pseudo-first-order kinetic model was also applied to describe the adsorption experimental data well with $R^2$ of 0.8389 (Appendix IX). The best-fit value of the adsorption rate constant kads was 0.00021$min^{-1}$, indicating the adsorption of MB onto g-$C_3N_4$ is not that much fast process. To determine the photodegradation kinetics of MB on g-$C_3N_4$ surface, the photocatalyst was first saturated with the contaminant in dark with MB solution at pH of 7. In comparison to that of MB adsorption it was difficult to determine the pure-photodegradation kinetics of MB in the bulk solution by g-$C_3N_4$ without the influence of adsorption. Therefore, the removal of MB by g-$C_3N_4$ at different time intervals at solution pH of 7 was used as the bulk degradation kinetics. Despite the influence of adsorption, simulations of the first-order model fairly described the experimental data with $R^2$ of 0.838. Based on the theoretical and kinetic model results, adsorption of contaminants onto g-$C_3N_4$ surface can accelerate photodegradation. On the other hand, photodegradation can also extend the adsorption capacity of g-$C_3N_4$ to contaminants[28].

Photocatalysis kinetics is used to evaluate the performance of a photocatalyst adsorbed MB solution which determines the contact time required for photocatalysis reaction may be established. The kinetics of photodegradation of MB at different time intervals given in Figure 4.16 was successful to remove methylene blue to about 67% in 60 mins. From the result shows after 40 min the MB removal/degradation very fast because initially the key recipient of the hydroxyl radials (OH.) is MB to undergo the oxidation reaction. However, later, smaller molecular fragments share or receive those radicals for oxidation and so the number of radicals becomes less available for MB resulting in lowering photodegradation rate.

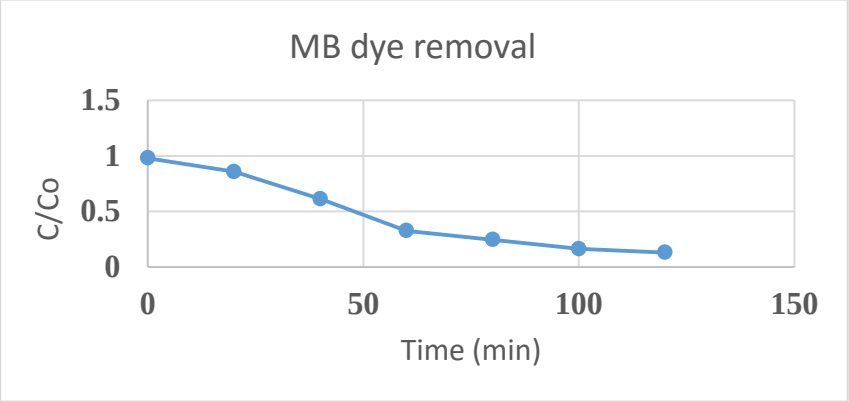


**Figure 4. 16 kinetic plot of ($C/C_o$) vs. irradiation time (min)**

### 4.6.1 Evaluation of the first order kinetic model

The photocatalytic degradation process as shown below is well-fitted by the pseudo-first-order kinetics (Eq. 10). Therefore, the pseudo-first-order rate constant (k) was determined from the plot t versus ln (qe – qt) used to compare the photodegradation efficiency of the catalysts. The result indicated pseudo-first-order kinetic model best explained the reaction process of MB degradation on the photocatalyst surface. As presented as table 4.10 with pseudo first order model, degradation amount of calculated equilibrium (qe) was very close to calculated (qt) at any time.

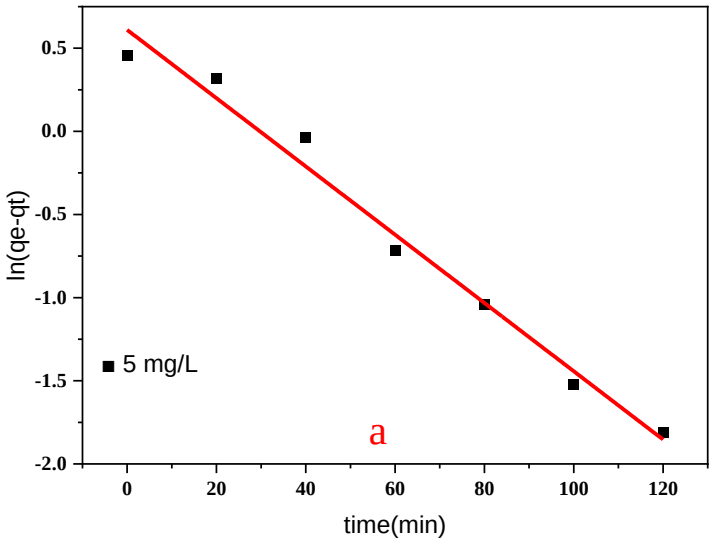


Figure 4. 17 plot of pseudo-first-order kinetic model

4.6.2 Evaluation of the second order kinetic mode

The second-order kinetic model plot is presented below in order to draw this plot, the t/qt values were taken from the optimum initial concentration of 5 mg/L. The value of $K_2$ was obtained from the plot of t versus t/qt.

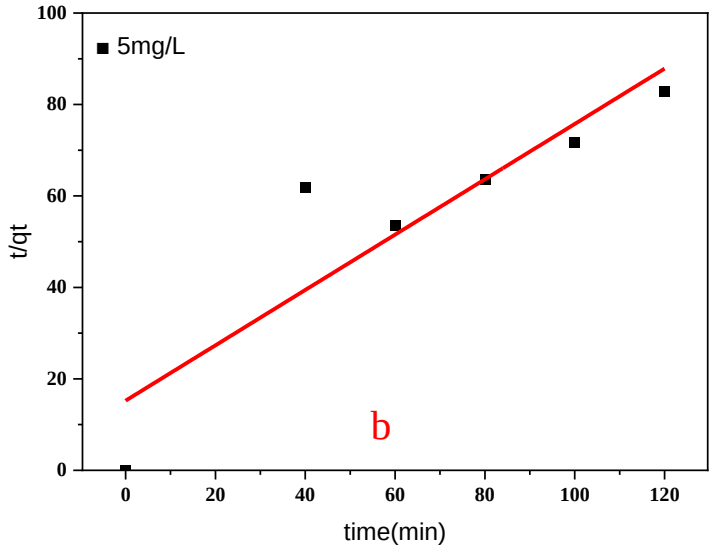


Figure 4. 18 plot of pseudo-second-order kinetic model

### 4.6.3 Evaluation of Inter-particle diffusion mode

The inter-particle diffusion kinetic parameter was determined from $t^{0.5}$ versus qt plot from (Equ.16). The values of the correlation coefficient $R^2$ were used to select the best reaction kinetic model. Table 4.10 presents the kinetic parameters of the selected kinetic models.

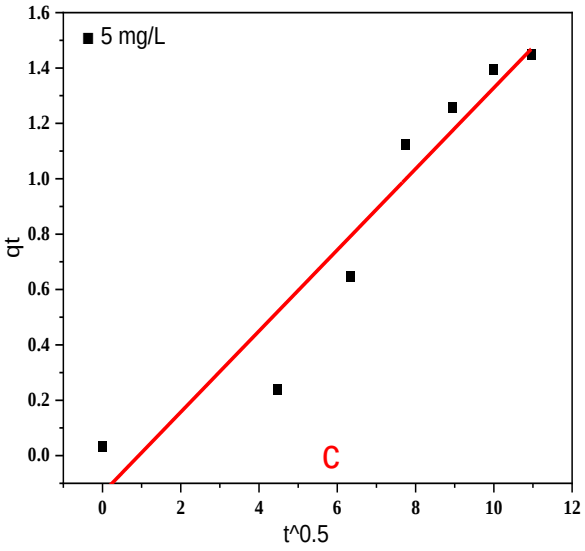


Figure 4. 19 plot of interparticle diffusion kinetic model

Table 4. 10 Pseudo-first-order, pseudo-second-order and interparticle diffusion kinetic models' parameters.

| Kinetic models | Parameters | Concentration (5 mg/L) |
|---|---|---|
| Pseudo-first-order | $K_1$ | 0.0002 |
| | qe cal | 1.656 |
| | qe exp | 1.449 |
| | $R^2$ | 0.962 |
| Pseudo-second-order | $K_2$ | 0.024 |
| | qe cal | 1.652 |
| | qe exp | 1.449 |
| | $R^2$ | 0.767 |
| Interparticle diffusion | Ki | 0.146 |
| | Ci | 0.136 |
| | $R^2$ | 0.905 |

## 5. Conclusions

The morphology and properties of $C_3N_4$ material strongly depend on the synthetic pathway, as well as on the precursor. Synthesis of g-$C_3N_4$ was conducted by thermal condensation of easily available precursor urea. XRD results indicated the crystal structure of g-$C_3N_4$ with two diffraction peaks around 2θ of 13.5° and 26.92°. On the whole,the average crystallite size according to Scherrer equation was found to be 2.7nm. The absorption bands in FT-IR spectra almost occurred at the same position for the samples obtained under different conditions. SEM observations found all material particles were in irregular shape grain clusters stacked disorderly that result caused by gas bubbles during pyrolysis of urea interconnected with thin layers. The PL spectra showed that all the samples had strong visible-light absorption edge around 424 nm, implying that all g-$C_3N_4$ photocatalysts exhibited visible-light response. Nitrogen adsorption–desorption measurements showed the specific surface area of as prepared sample 54.9 $m^2/g$. Different reaction parameters or experimental conditions including pH, the concentration of pollutant, dose of the adsorbent or photo-catalyst, and temperature Particularly, a retainable pyrolysis-generated self-supporting atmosphere and the reaction temperature are the two vital parameters for the successful synthesis of g-$C_3N_4$. to see the effect of such different reaction parameters on $C_3N_4$ materials and the interaction effect of the variables determined by the statistical model developed through RSM Approach with a three-factor BBD was found to be reliable for modeling of photocatalytic degradation of MB by using graphitic carbon nitride((g-$C_3N_4$) material. The statistical model accuracy and fitness was evaluated using ANOVA.The Freundlich and Langmuir adsorption models were used to elucidate the adsorption efficiency of g-$C_3N_4$. The kinetic data depicts the pseudo first, second, and inter-particle diffusion model. Adsorption and kinetic isotherm showed that the adsorption process can be well described by pseudo-first -order kinetic model, with an adsorption capacity of 552 mg MB per gram adsorbent determined by Langmuir isotherm.

## 6. Recommendations

The application of graphitic carbon nitride materials for photocatalysis and adsorption capacity has achieved great achievements over the years. It has a highly stable basic framework and excellent structural parameters, which can be used to remove various toxic molecules and replace existing low-efficiency adsorption materials, but there are still many challenges in the application of this material in catalysis. First, it is necessary to increase the surface area of g-$C_3N_4$. The purely prepared g-$C_3N_4$ material has a low surface area, which reduces its catalytic activity. Although it is possible to obtain g-$C_3N_4$ with improved surface area by the template method or the introduction of heteroatoms (metallic and non-metallic doping) in the framework of g-$C_3N_4$, metal deposition, hybridization with carbon nanomaterials and the Coupling with other semiconductors has always been the most important, attractive method for producing heterostructures with enhanced photocatalytic activity for large scale application. Correct selection and pyrolysis of the template are essential for the complete and successful synthesis of g-$C_3N_4$. Otherwise, the template material decomposes before the formation of g-$C_3N_4$ and eventually increases the carbon residue in the final product. The mineralization ability of the catalyst or reduction of TOC in photodegradation process not investigated in this study. Future research should pay attention to mineralization analysis by the help of advanced TOC analyzer. All these efforts together with the substantial ongoing progress in the field will make CN materials competitive candidate photo catalysts or semiconductors for many environmental remediation, energy-related applications and more in the future.

**References**


[1] M. Fakhrul, R. Samsudin, and N. Bacho, "Recent Development of Graphitic Carbon Nitride-Based Photocatalyst for Environmental Pollution Remediation," no. 2003, pp. 1–15.

[2] G. Crini and E. Lichtfouse, "Advantages and disadvantages of techniques used for wastewater treatment," *Environmental Chemistry Letters*, vol. 17, no. 1, pp. 145–155, 2019, doi: 10.1007/s10311-018-0785-9.

[3] M. T. Amin, A. A. Alazba, and U. Manzoor, "A review of removal of pollutants from water/wastewater using different types of nanomaterials," *Advances in Materials Science and Engineering*, vol. 2014, 2014, doi: 10.1155/2014/825910.

[4] Z. Yang, Y. Zhang, and Z. Schnepp, "Soft and hard templating of graphitic carbon nitride," *Journal of Materials Chemistry A: Materials for energy and sustainability*, vol. 00, pp. 1–12, 2015, doi: 10.1039/C5TA02156A.

[5] A. Manuscript, "Nanoscale Biological Applications : A Review," 2019, doi: 10.1039/C9NR04568F.

[6] D. Chatterjee and S. Dasgupta, "Visible light induced photocatalytic degradation of organic pollutants," vol. 6, pp. 186–205, 2005, doi: 10.1016/j.jphotochemrev.2005.09.001.

[7] F. Dong, Z. Wang, Y. Sun, W. K. Ho, and H. Zhang, "Engineering the nanoarchitecture and texture of polymeric carbon nitride semiconductor for enhanced visible light photocatalytic activity," *Journal of Colloid and Interface Science*, vol. 401, pp. 70–79, 2013, doi: 10.1016/j.jcis.2013.03.034.

[8] Z. Chen *et al.*, "Synthesis and fabrication of g-C3N4-based materials and their application in elimination of pollutants," *Science of the Total Environment*, vol. 731, p. 139054, 2020, doi: 10.1016/j.scitotenv.2020.139054.

[9] G. Xin and Y. Meng, "Pyrolysis Synthesized g-C 3 N 4 for Photocatalytic Degradation of Methylene Blue," vol. 2013, 2013.

[10] X. Wang *et al.*, "A metal-free polymeric photocatalyst for hydrogen production from water under visible light," *Nature Materials*, vol. 8, no. 1, pp. 76–80, 2008, doi: 10.1038/nmat2317.

[11] F. Goettmann, A. Fischer, M. Antonietti, and A. Thomas, "Chemical Synthesis of Mesoporous Carbon Nitrides Using Hard Templates and Their Use as a Metal-Free

Catalyst for Friedel–Crafts Reaction of Benzene**," pp. 4467–4471, 2006, doi: 10.1002/anie.200600412.

[12] J. Liu, H. Wang, and M. Antonietti, "Chem Soc Rev applications beyond (photo) catalysis," pp. 2308–2326, 2016, doi: 10.1039/c5cs00767d.

[13] S. Yang *et al.*, "Exfoliated Graphitic Carbon Nitride Nanosheets as Effi cient Catalysts for Hydrogen Evolution Under Visible Light," pp. 2452–2456, 2013, doi: 10.1002/adma.201204453.

[14] P. Niu, L. Zhang, G. Liu, and H. Cheng, "Graphene-Like Carbon Nitride Nanosheets for Improved Photocatalytic Activities," pp. 4763–4770, 2012, doi: 10.1002/adfm.201200922.

[15] G. Algara-siller *et al.*, "Semiconductor **," pp. 1–6, 2014, doi: 10.1002/anie.201402191.

[16] A. Wang, C. Wang, L. Fu, and W. W. Yucheng, "Recent Advances of Graphitic Carbon Nitride-Based Structures and Applications in Catalyst, Sensing, Imaging, and LEDs," 2017, doi: 10.1007/s40820-017-0148-2.

[17] J. Bian, Q. Li, C. Huang, J. Li, and Y. Guo, "Thermal vapor condensation of uniform graphitic carbon nitride fi lms with remarkable photocurrent density for photoelectrochemical applications," *Nano Energy*, pp. 1–8, 2015, doi: 10.1016/j.nanoen.2015.04.012.

[18] L. H. Amorin *et al.*, "Electronic, structural, optical, and photocatalytic properties of graphitic carbon nitride," *New Journal of Chemistry*, vol. 43, no. 34, pp. 13647–13653, 2019, doi: 10.1039/c9nj02702e.

[19] J. Huang and J. Liu, "Bio-inspired carbon nitride mesoporous spheres for arti fi cial photosynthesis : photocatalytic cofactor regeneration for sustainable enzymatic synthesis †," pp. 7686–7693, 2014, doi: 10.1039/c4ta00793j.

[20] I. F. Teixeira, E. C. M. Barbosa, and P. H. C. Camargo, "Chem Soc Rev Carbon nitrides and metal nanoparticles: from controlled synthesis to design principles for improved photocatalysis," 2019, doi: 10.1039/c8cs00479j.

[21] F. Paquin, J. Rivnay, A. Salleo, N. Stingelin, and C. Silva, "Multi-phase semicrystalline microstructures drive exciton dissociation in neat plastic semiconductors," *J. Mater. Chem. C*, vol. 3, pp. 10715–10722, 2015, doi: 10.1039/b000000x.

[22] S. Kumar, S. Karthikeyan, and A. F. Lee, "g-C3N4-based nanomaterials for visible light-driven photocatalysis," *Catalysts*, vol. 8, no. 2, 2018, doi: 10.3390/catal8020074.

[23] M. Tahir *et al.*, “Tubular graphitic-C3N4: A prospective material for energy storage and green photocatalysis,” *Journal of Materials Chemistry A*, vol. 1, no. 44, pp. 13949–13955, 2013, doi: 10.1039/c3ta13291a.

[24] G. Mamba and A. K. Mishra, “Graphitic carbon nitride (g-C3N4) nanocomposites: A new and exciting generation of visible light driven photocatalysts for environmental pollution remediation,” *Applied Catalysis B: Environmental*, vol. 198, pp. 347–377, 2016, doi: 10.1016/j.apcatb.2016.05.052.

[25] M. Volokh and M. Shalom, “materials for energy and environmental,” 2020, doi: 10.1039/d0ta01973a.

[26] B. Tiwari and S. Ram, “Biogenic Synthesis of Graphitic Carbon Nitride for Photocatalytic Degradation of Organic Dyes,” *ACS Omega*, vol. 4, no. 6, pp. 10263–10272, 2019, doi: 10.1021/acsomega.9b00989.

[27] G. Goglio, D. Foy, and G. Demazeau, “State of Art and recent trends in bulk carbon nitrides synthesis,” *Materials Science and Engineering R: Reports*, vol. 58, no. 6, pp. 195–227, 2008, doi: 10.1016/j.mser.2007.10.001.

[28] Y. Luo *et al.*, “Synergistic adsorption-photocatalysis processes of graphitic carbon nitrate (g-C3N4) for contaminant removal: Kinetics, models, and mechanisms,” *Chemical Engineering Journal*, vol. 375, no. June, p. 122019, 2019, doi: 10.1016/j.cej.2019.122019.

[29] Q. Chen *et al.*, “Enhanced visible-light driven photocatalytic activity of hybrid ZnO/g-C3N4 by high performance ball milling,” *Journal of Photochemistry and Photobiology A: Chemistry*, vol. 350, pp. 1–9, 2018, doi: 10.1016/j.jphotochem.2017.09.015.

[30] F. Chang, C. Li, J. Luo, Y. Xie, B. Deng, and X. Hu, “Enhanced visible-light-driven photocatalytic performance of porous graphitic carbon nitride,” *Applied Surface Science*, vol. 358, pp. 270–277, 2015, doi: 10.1016/j.apsusc.2015.08.124.

[31] H. Swenson and N. P. Stadie, “Langmuir’s Theory of Adsorption: A Centennial Review,” *Langmuir*, vol. 35, pp. 5409–5426, 2019, doi: 10.1021/acs.langmuir.9b00154.

[32] Nimibofa Ayawei et al., “Modelling and Interpretation of Adsorption Isotherms,” *Journal of Chemistry*, vol. 2017, pp. 1–11, 2017, doi: https://doi.org/10.1155/2017/3039817.

[33] T. R. Sahoo and B. Prelot, “Adsorption processes for the removal of contaminants from wastewater,” *Nanomaterials for the Detection and Removal of Wastewater Pollutants*, pp. 161–222, 2020, doi: 10.1016/b978-0-12-818489-9.00007-4.

[34] Y. Li *et al.*, “Macroscopic Foam-Like Holey Ultrathin g-C3N4 Nanosheets for Drastic Improvement of Visible-Light Photocatalytic Activity,” *Advanced Energy Materials*, vol. 6, no. 24, pp. 1–5, 2016, doi: 10.1002/aenm.201601273.

[35] S. Zhang *et al.*, “In-situ fabrication of g-c3n4/zno nanocomposites for photocatalytic degradation of methylene blue: Synthesis procedure does matter,” *Nanomaterials*, vol. 9, no. 2, 2019, doi: 10.3390/nano9020215.

[36] X. Song, Q. Yang, M. Yin, D. Tang, and L. Zhou, “Highly efficient pollutant removal of graphitic carbon nitride by the synergistic effect of adsorption and photocatalytic degradation,” *RSC Advances*, vol. 8, no. 13, pp. 7260–7268, 2018, doi: 10.1039/c7ra11467b.

[37] D. Saha *et al.*, “Influence of Hydrogen Peroxide in Enhancing Photocatalytic Activity of Carbon Nitride Under Visible Light: An Insight into Reaction Intermediates,” pp. 1–28.

[38] B. Gebregziabher, S. K. Kassahun, and Z. Kiflie, “Statistical optimization of mixed peanut shell and Khat (Catha edulis) stem carbonization process for molasses enhanced cold and low-pressure pelletization,” 2021.

[39] H. Lee, J. Hur, Y. Hwang, and H. Shin, “A Novel Procedure of Total Organic Carbon Analysis for Water Samples Containing Suspended Solids with Alkaline Extraction and Homogeneity Evaluation by Turbidity,” 2020.

[40] H. Ashra, M. Akhond, and G. Absalan, “Journal of Photochemistry & Photobiology A: Chemistry Adsorption and photocatalytic degradation of aqueous methylene blue using nanoporous carbon nitride,” vol. 396, no. March, 2020, doi: 10.1016/j.jphotochem.2020.112533.

[41] Jemal Fito et al., “Fluoride removal from aqueous solution onto activated carbon of Catha edulis through the adsorption treatment technology,” *Environmental Systems Research*, vol. 8, no. 1, pp. 1–10, 2019, doi: 10.1186/s40068-019-0153-1.

# Appendixes

## Appendix I BET analysis as prepared samples 550 $^{o}$C-3hrs and 550 $^{o}$C-4hrs ,500 $^{o}$C-3hrs and 550 $^{o}$C -4hrs.

**Horiba Instruments, Inc.**
SA-9600 Series Surface Area Analyzer

**Analysis Report**
Aug/30/2021

| | | | |
|---|---|---|---|
| Customer | : Eyerusalem Ayalkibe | Operator ID | : SARA, CHEMO |
| Description | : Different Experiment | Analysis Date | : Aug/30/2021 |
| Filename | : eyerusalem 4.xps | Analysis Time | : 13:02:04 |

**Condition Settings**

| | | | |
|---|---|---|---|
| Room Temp | : 27.0 (°C) | Atm. Pres | : 700.0 (mm) |
| Gas Used | : Nitrogen | Gas Conc | : 0.500, 0.002, 0.002 % |

| | Channel: 1 | Channel: 2 | Channel: 3 |
|---|---|---|---|
| Sample Name | 550 OC / 3 HRS | 550 OC / 4 HRS | |
| Tube Number | 1 | 2 | 0 |
| Tare Weight | 10.0730 (gm) | 10.0100 (gm) | 0.0000 (gm) |
| Sample Weight | 10.1540 (gm) | 10.0840 (gm) | 1.0000 (gm) |
| Degas Temp. | 100 (°C) | 100 (°C) | 0 (°C) |
| Degas Time | 60 (min) | 60 (min) | 0 (min) |
| Surface Area (M²/gm) | 53.532 | 54.855 | -1.#IO |
| Slope | 796.593 | 851.185 | -1.#IO |
| Intercept | 5.967 | 6.122 | -1.#IO |
| Vm | 0.001 | 0.001 | -1.#IO |
| BET Const | 134.506 | 140.044 | -1.#IO |
| Pearson Coef | 1.000 | 1.000 | 0.000 |
| X[1] - 0.449 | 363.933 | 388.821 | 1.#IO |
| X[2] - 0.269 | 218.872 | 233.016 | 1.#IO |
| X[3] - 0.179 | 149.986 | 160.413 | 1.#IO |

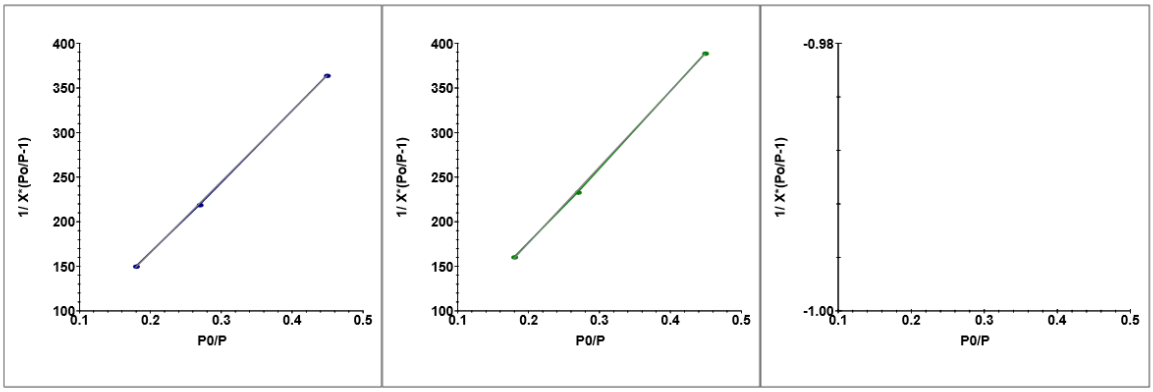

**Horiba Instruments, Inc.**
SA-9600 Series Surface Area Analyzer

**Analysis Report**
Aug/27/2021

| | | | |
|---|---|---|---|
| Customer | : Eyerusalem Ayalkibe | Operator ID | : SARA, CHEMO |
| Description | : Different Experiment | Analysis Date | : Aug/27/2021 |
| Filename | : eyelusalem 1.sa2 | Analysis Time | : 11:59:08 |

**Condition Settings**

| | | | |
|---|---|---|---|
| Room Temp | : 28.0 (°C) | Atm. Pres | : 700.0 (mm) |
| Gas Used | : Nitrogen | Gas Conc | : 0.500, 0.002, 0.002 % |

| | Channel: 1 | Channel: 2 | Channel: 3 |
|---|---|---|---|
| Sample Name | 500 OC / 3 HRS | 500 OC / 4 HRS | |
| Tube Number | 1 | 2 | 0 |
| Tare Weight | 10.1310 (gm) | 10.1100 (gm) | 0.0000 (gm) |
| Sample Weight | 10.1970 (gm) | 10.1770 (gm) | 0.0000 (gm) |
| Degas Temp. | 100 (°C) | 100 (°C) | 0 (°C) |
| Degas Time | 60 (min) | 60 (min) | 0 (min) |
| Surface Area (M²/gm) | 46.312 | 46.123 | 0.000 |
| Slope | 1141.326 | 1125.630 | -1.#IO |
| Intercept | -2.807 | 0.482 | -1.#IO |
| Vm | 0.001 | 0.001 | -1.#IO |
| BET Const | -405.569 | 2336.894 | -1.#IO |
| Pearson Coef | 1.000 | 1.000 | 0.000 |
| X[1] - 0.449 | 509.650 | 506.193 | 1.#IO |
| X[2] - 0.269 | 303.501 | 301.674 | 1.#IO |
| X[3] - 0.179 | 202.694 | 203.759 | 1.#IO |

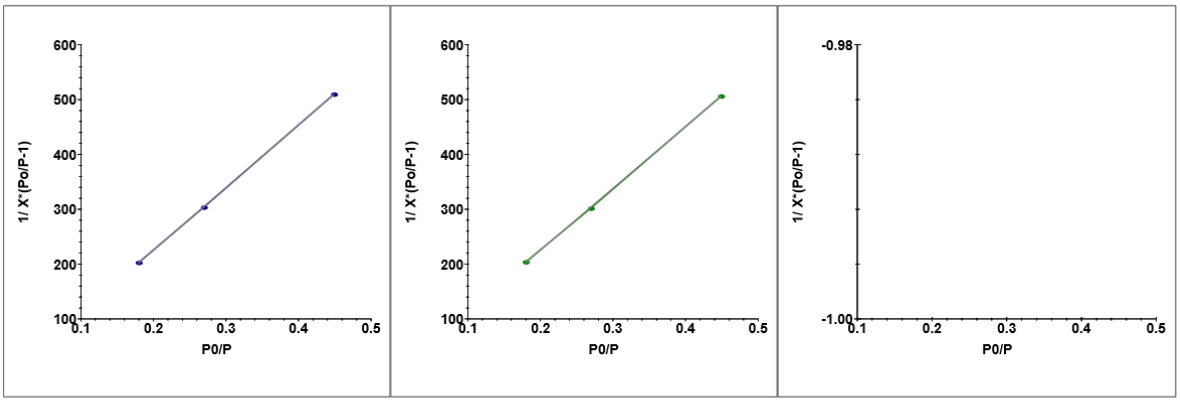

## Appendix II Calibration Curve for standard solution

| Absorbance | Concentration |
|---|---|
| 0 | 0 |
| 0.003 | 1 |
| 0.01 | 2 |
| 0.015 | 4 |
| 0.028 | 6 |
| 0.037 | 8 |
| 0.054 | 10 |

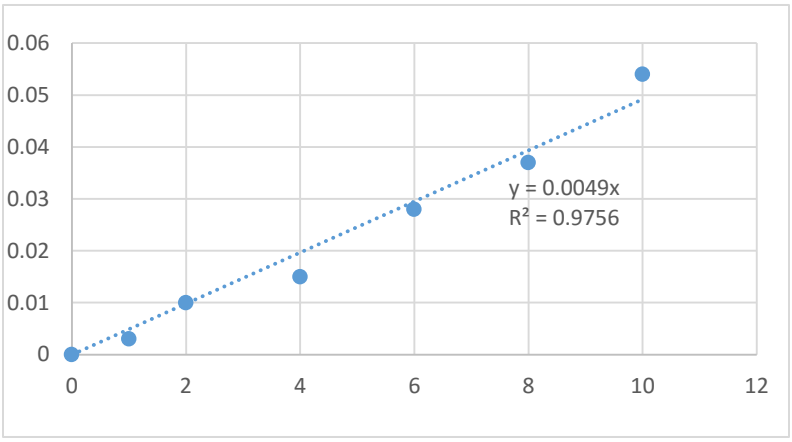


## Appendix III Some important captured photos during experimental works.


1. Synthesis of g-$C_3N_4$ using extra pure urea calcine in furnace

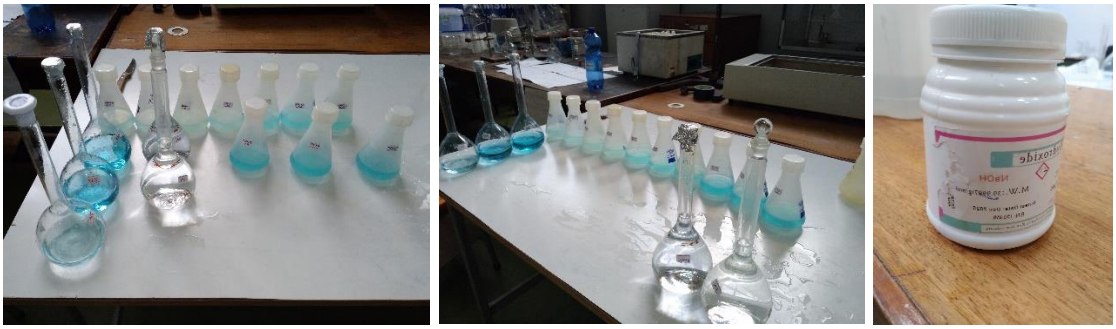

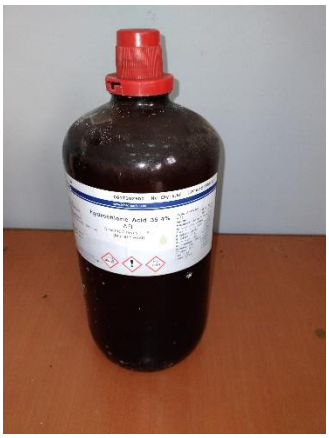

2. Prepared stock solutions and sample runs with adjusted pH

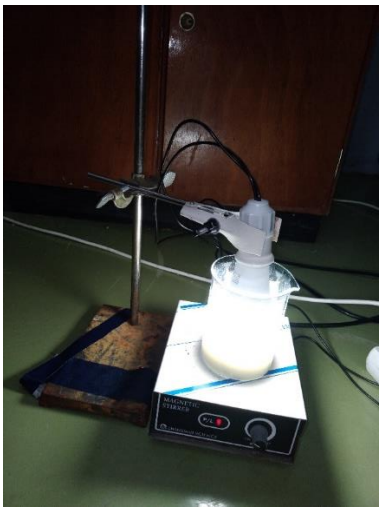

3. Photocatalytic process in dark and visible light irradiation conditions



4. Digital weighing machine and UV-Spectrophotometer for Samples analysis

## Appendix IV Langmuir Adsorption Isotherm fit curve statistics

| | |
|---|---|
| Equation | y = a + b*x |
| Plot | Ce /qe |
| Weight | No Weighting |
| Intercept | -0.00103 ± 3.34551E-4 |
| Slope | 0.00181 ± 1.95588E-4 |
| Residual Sum of Squares | 4.26131E-7 |
| Pearson's r | 0.98294 |
| R-Square (COD) | 0.96617 |
| Adj. R-Square | 0.95489 |

## Appendix V Freundlich Adsorption Isotherm fit curve statistics

| | |
|---|---|
| Equation | y = a + b*x |
| Plot | log qe |
| Weight | No Weighting |
| Intercept | 0.11643 ± 0.17743 |
| Slope | -1.43859 ± 0.42734 |
| Residual Sum of Squares | 0.66234 |
| Pearson's r | -0.83299 |
| R-Square (COD) | 0.69387 |
| Adj. R-Square | 0.63264 |

## Appendix VI pseudo-first-order equation statistics for photocatalysis

| | |
|---|---|
| Equation | y = a + b*x |
| Plot | ln(qe-qt) |
| Weight | No Weighting |
| Intercept | 0.5047 ± 0.15534 |
| Slope | -0.02655 ± 0.00305 |
| Residual Sum of Squares | 0.07425 |
| Pearson's r | -0.98709 |
| R-Square (COD) | 0.97434 |
| Adj. R-Square | 0.96151 |

## Appendix VII pseudo-second order equation statistics for photocatalysis

| | |
|---|---|
| Equation | y = a + b*x |
| Plot | t/qt |
| Weight | No Weighting |
| Intercept | 15.23192 ± 11.20805 |
| Slope | 0.60512 ± 0.1447 |
| Residual Sum of Squares | 781.63745 |
| Pearson's r | 0.90214 |
| R-Square (COD) | 0.81386 |
| Adj. R-Square | 0.76733 |

## Appendix VIII Interparticle diffusion model statistics for photocatalysis

| | |
|---|---|
| Equation | y = a + b*x |
| Plot | Qt |
| Weight | No Weighting |
| Intercept | -0.13559 ± 0.1485 |
| Slope | 0.1464 ± 0.01917 |
| Residual Sum of Squares | 0.15579 |
| Pearson's r | 0.9597 |
| R-Square (COD) | 0.92103 |
| Adj. R-Square | 0.90524 |

## Appendix IX pseudo-first-order equation statistics for adsorption process

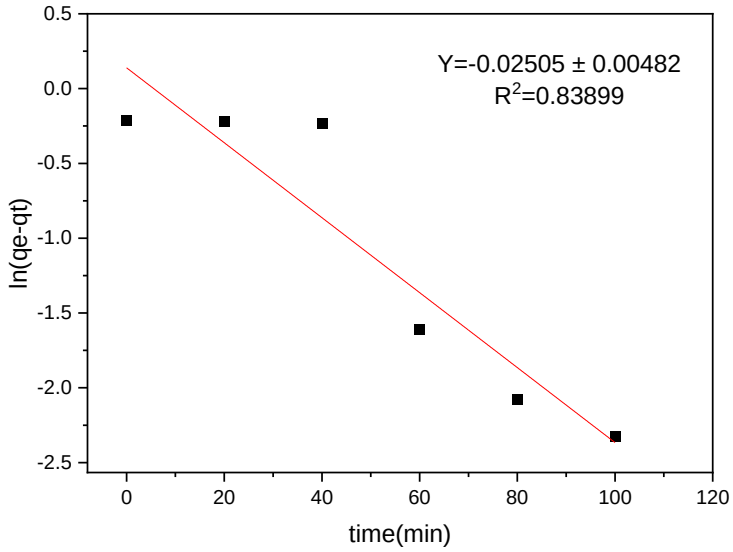


| | |
|---|---|
| Equation | y = a + b*x |
| Plot | ln(qe-qt) |
| Weight | No Weighting |
| Intercept | 0.13919 ± 0.29163 |
| Slope | -0.02505 ± 0.00482 |
| Residual Sum of Squares | 0.64946 |
| Pearson's r | -0.93338 |
| R-Square (COD) | 0.87119 |
| Adj. R-Square | 0.83899 |

Appendix X Experimental data for Langmuir and Freundlich Adsorption Isotherm model (for adsorption process) and adsorption efficiency calculation

| Time | Absorbance | Ce | Qe | log Ce | log qe |
|---|---|---|---|---|---|
| 0 | 0.02345 | 4.785714286 | 0.071428571 | 0.67995 | -1.1461 |
| 20 | 0.0234 | 4.775510204 | 0.074829932 | 0.67902 | -1.1259 |
| 40 | 0.0232 | 4.734693878 | 0.088435374 | 0.67529 | -1.0534 |
| 60 | 0.0145 | 2.959183673 | 0.680272109 | 0.47117 | -0.1673 |
| 80 | 0.0134 | 2.734693878 | 0.755102041 | 0.43691 | -0.122 |
| 100 | 0.013 | 2.653061224 | 0.782312925 | 0.42375 | -0.1066 |
| 120 | 0.0115 | 2.346938776 | 0.884353741 | 0.3705 | -0.0534 |